Unraveling the Effect of the Chemical and Structural Composition of ZnxNi1xFe2O4 on the Electron Transfer at the Electrochemical Interface

Original
Unraveling the Effect of the Chemical and Structural Composition of ZnxNi1xFe2O4 on the Electron Transfer at the Electrochemical Interface / Madagalam, M., Bartoli, M., Rosito, M., Blangetti, N., ETZI COLLER PASCUZZI, M., Padovano, E., Bonelli, B., Carrara, S., Tagliaferro, A.. - In: SMALL STRUCTURES. - ISSN 2688-4062. - 4:12(2023). [10.1002/sstr.202300163]

Publisher:
Wiley-VCH

Published
DOI:10.1002/sstr.202300163

Unraveling the Effect of the Chemical and Structural Composition of $Zn_xNi_{1-x}Fe_2O_4$ on the Electron Transfer at the Electrochemical Interface

Mallikarjun Madagalam, Mattia Bartoli, Michele Rosito, Nicola Blangetti, Marco Etzi Coller Pascuzzi, Elisa Padovano, Barbara Bonelli, Sandro Carrara, and Alberto Tagliaferro*

In order to deepen the understanding of the role of transition metal oxides in electron transfer at the electrochemical interface, the performance of $Zn_xNi_{1-x}Fe_2O_4$ ($x = 0$, 0.2, 0.4, 0.6, 0.8, 1) nanomaterials in electrochemical sensing is studied. Nanomaterials are synthesized by simple autocombustion synthesis procedure. Field-emission scanning electron microscopy characterization shows that the particles have a size between 30 and 70 nm with an average crystallite size between 24 and 35 nm. The bandgap energies of the nanomaterials, as estimated by UV–vis experiments, are in the 2.32–2.56 eV range. The valence band maximum is evaluated using X-ray photoelectron spectroscopy and the position of the conduction band minimum is estimated. The $ZnFe_2O_4$ sensor has the best performances: highest rate constant ($13.1 \pm 2.8\ ms^{-1}$), lowest peak-to-peak separation (386 ± 2 mV), and highest sensitivity ($37.75 \pm 0.17\ \mu A\ mM^{-1}$). Its limit of detection ($7.94 \pm 0.04\ \mu M$) is second best, and its sensitivity is more than twice the sensitivity of the bare sensor ($16.7 \pm 0.9\ \mu A\ mM^{-1}$). Nanomaterials energy bands mapping with the experimental redox potentials is performed to predict the electron transfer at the electrochemical interface, and the importance of surface states/defects is highlighted in the electron transfer mechanism.

1. Introduction

The large group of oxides with the AB_2O_4 formula is known as the spinel group.[1] In a spinel unit cell, 32 oxygen anions with face-centered cubic (FCC) cell form 64 tetrahedral sites (a site or void due to 4 oxygen anions), and 32 octahedral sites (a site or void due to 6 oxygen anions), 8 units of AB_2O_4 form a unit cell with $8'+2'$ cations and $16'+3'$ cations occupying 8 tetrahedral and 16 octahedral sites, respectively, forming a cubic close-packed (CCP) system resulting an electrically neutral structure. Spinel can be normal spinel, inverse spinel, and partially inverse/normal spinel depending on the site occupancy of the cations present in the system.

A general spinel structure formula can be written as $(A^{+2}{}_{1-x}B^{+3}{}_{x})_{Td}(A^{+2}{}_{x}B^{+3}{}_{2-x})_{Oh}O_4$, where "Td" is the tetrahedral site and "Oh" is the octahedral site, respectively. Spinel ferrite is a spinel with "B" as Fe if Fe(III) occupies all the "Oh" sites and A(II) occupies all the "Td" sites (i.e., $x = 0$) is referred to as normal spinel ferrite (e.g., $ZnFe_2O_4$ (Franklinite)). If $x = 1$, then it is an inverse spinel ferrite (e.g., $NiFe_2O_4$ (Trevorite), Fe_3O_4 (magnetite) with Fe(II) and Fe(III)) where the "Oh" sites are shared between A(II) and Fe(III) ions. The third case is where "Td" and "Oh" sites are shared between A(II) and Fe(III) ions with $0 < x < 1$ (e.g., $Zn_{1-x}Ni_xFe_2O_4$), based on the fraction "x" of Zn/Ni the structure is referred to as partially normal spinel or partially inverse spinel, respectively.[2–7]

M. Madagalam, M. Rosito, N. Blangetti, E. Padovano, B. Bonelli,
A. Tagliaferro
Department of Applied Science and Technology
Politecnico di Torino
Duca degli Abruzzi 24, 10129 Torino, Italy
E-mail: mallikarjun.madagalam@polito.it

The ORCID identification number(s) for the author(s) of this article can be found under https://doi.org/10.1002/sstr.202300163.

DOI: 10.1002/sstr.202300163

M. Madagalam, S. Carrara
Bio/CMOS Interfaces Laboratory
École Polytechnique Fédérale de Lausanne
Rue de la Maladière 71b, 2000 Neuchâtel, Switzerland

M. Madagalam, M. Bartoli, E. Padovano, B. Bonelli, A. Tagliaferro
National Interuniversity Consortium of Materials Science and Technology
Unit of Torino – Politecnico di Torino
Via Giuseppe Giusti, 9, 50121 Florence, Italy

M. Bartoli, M. Etzi Coller Pascuzzi
Center for Sustainable Future Technologies
Fondazione Istituto Italiano di Tecnologia
Via Livorno 60, 10144 Torino, Italy

$ZnFe_2O_4$ (normal spinel)[8–10] and $NiFe_2O_4$ (inverse spinel)[5–7,11] are among the most studied due to their high thermal and chemical stability, and electrical neutrality. The synthesis method plays a crucial role in obtaining the desired properties of spinel ferrites; different types of synthesis methods have been explored following dry and wet routes. Dry synthesis mainly includes the combustion method,[12,13] while wet synthesis follows so many methods including sol–gel autocombustion,[5,14] coprecipitation method,[6] solvent deficient method,[15] and the sonochemical method.[16,17]

The use of spinel ferrites nanomaterials has emerged as a performing approach to produce new catalytic materials in electrochemical applications such as energy storage,[18,19] supercapacitors,[20,21] fuel cells,[22,23] and electrochemical sensors.[24,25] Ferrite-based electrochemical sensors on different carbon-based platforms such as carbon paste, glassy carbon, and screen-printed carbon electrodes have been studied in sensing different biomolecules over the years.[15,26–28] Several authors[24,25] deeply investigated the synthesis methods and electrochemical sensing applications of MFe_2O_4 (M = Mg, Ni, Co, Mn, Cu, and Zn). Among the several species, $ZnFe_2O_4$ was the most performing and it was used in electrochemical sensors as a sensing material for the detection of dopamine,[29] H_2O_2,[30–32] heavy metals Hg^{+2}, Pb^{+2}, Cu^{+2}, and glucose[26,33] while $NiFe_2O_4$ in sensing nitrite,[15] paracetamol, acetone, folic acid,[17,34–36] H_2O_2,[37] and glucose.[38,39]

This work presents the role of $Zn_xNi_{1-x}Fe_2O_4$ ($x = 0, 0.2, 0.4, 0.6, 0.8, 1$) nanomaterials as sensing materials in electrochemical sensors to clarify the complex relationship between chemical and structural features with electron transfer at the electrochemical interface. Materials were synthesized by a simple, effective, single-step autocombustion method to achieve a regular spherical shape. Energy bandgap, conduction band, and valence band edge energies were estimated, to predict the electron transfer at the electrochemical interface by mapping with the redox potentials of analyte species. Commercially available screen-printed carbon electrodes (SPCE) are used as electrochemical support to use $Zn_xNi_{1-x}Fe_2O_4$ as sensing materials. Paracetamol was chosen to be a model drug to demonstrate the performance of the obtained electrochemical sensors as drug detectors. In particular, two different crystal structures have been studied as affecting the sensitivity, and the first-order kinetic rate constant in electrochemical sensing through cyclic voltammetry (CV). Sensitivity (S), electron transfer rate coefficient (α), kinetic rate constant (k), and limit of detection (LOD) of the bare and $Zn_xNi_{1-x}Fe_2O_4$ sensors are reported and discussed.

2. Results

2.1. Materials Characterization

2.1.1. Morphological and Structural Characterization

Field-emission scanning electron microscopy (FESEM) technique was employed to investigate the synthesized materials' size and morphology. As reported in **Figure 1**, $Zn_xNi_{1-x}Fe_2O_4$ materials are spherical-shaped particles aggregated in clusters. The aggregation of particles is quite possible due to the autocombustion synthesis method used; the morphology of the nanoparticles is in clear agreement with the morphology of ferrite materials reported in the literature.[12,13] Particle size is estimated from Figure 1 by statistics on particles for each material using ImageJ software, an estimated average particle size of each material is reported in **Table 1** which varies between 30 and 70 nm. We observe variations in particle size by the addition of Zn into the structure of $NiFe_2O_4$. This is evident from the SEM images in

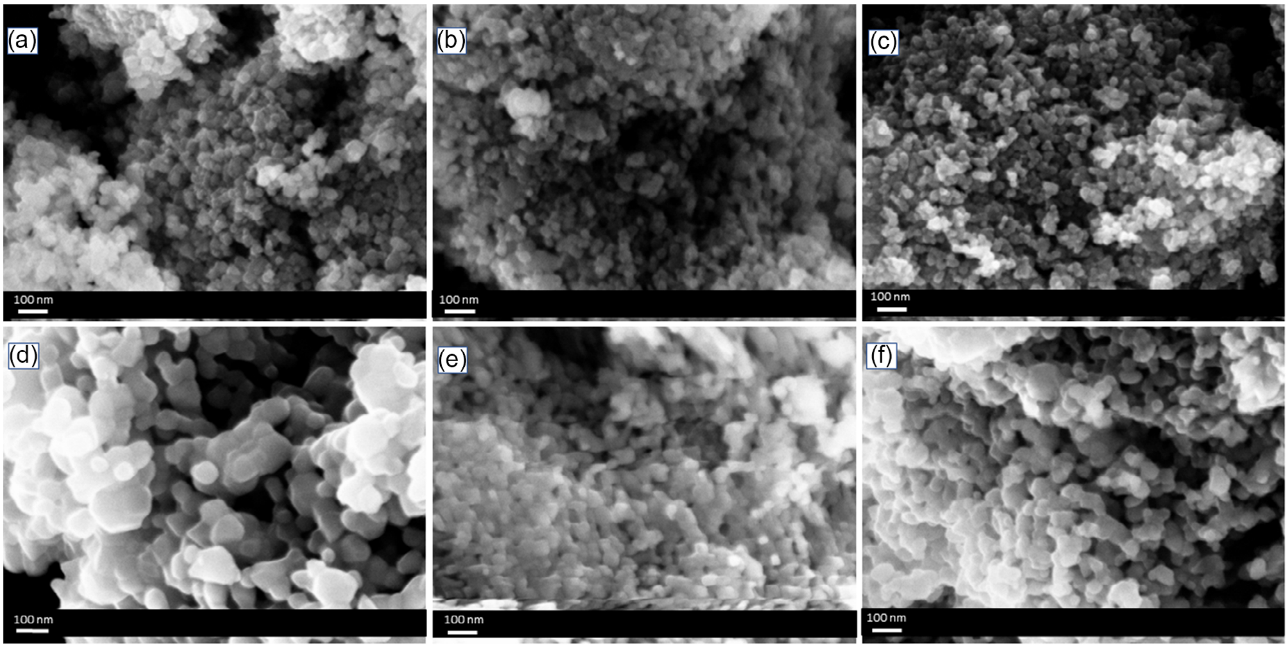

Figure 1. FE-SEM images of a) $NiFe_2O_4$, b) $Ni_{0.8}Zn_{0.2}Fe_2O_4$, c) $Ni_{0.6}Zn_{0.4}Fe_2O_4$, d) $Ni_{0.4}Zn_{0.6}Fe_2O_4$, e) $Ni_{0.2}Zn_{0.8}Fe_2O_4$, and f) $ZnFe_2O_4$ particles, respectively, produced by autocombustion synthesis.

Table 1. The average particle size of $Zn_xNi_{1-x}Fe_2O_4$ nanomaterials.

Material	Particle size [nm]
$NiFe_2O_4$	35 ± 6
$Ni_{0.8}Zn_{0.2}Fe_2O_4$	39 ± 8
$Ni_{0.6}Zn_{0.4}Fe_2O_4$	31 ± 7
$Ni_{0.4}Zn_{0.6}Fe_2O_4$	66 ± 18
$Ni_{0.2}Zn_{0.8}Fe_2O_4$	36 ± 9
$ZnFe_2O_4$	44 ± 17

Figure 1a–f that the particles are aggregated, and estimating the exact size is difficult. From Figure 1d,f the particles are larger in size compared to the particles in Figure 1a–c,e. It is possible that some of the particles were formed by more crystallites as there is no control over the particle size and shape due to the synthesis method used. Keeping this in mind it was possible that $Ni_{0.4}Zn_{0.6}Fe_2O_4$ and $ZnFe_2O_4$ were formed by more crystallites compared to $Zn_xNi_{1-x}Fe_2O_4$ ($x = 0$, 0.8, 0.4, 0.2) nanomaterials. Considering the standard deviation in particle size $Zn_xNi_{1-x}Fe_2O_4$ ($x = 0$, 0.8, 0.4, 0.2) nanomaterials have similar particle size whereas $Ni_{0.4}Zn_{0.6}Fe_2O_4$ is slightly higher than the $ZnFe_2O_4$ particle size.

Figure 2 shows the FESEM images of the surface of the $ZnFe_2O_4$-modified carbon working electrode (WE). Figure 2a shows the $ZnFe_2O_4$ particles dispersed carbon WE; it is clear from the figure that the dispersed particles are nanoparticles with some degree of aggregation. The size of particles was deduced from Figure 2b using ImageJ, a portion with less aggregation of particles in the image was selected and scaled to visualize the particles at the nanoscale. Line operator was used to estimate the diameter of 30 different particles and the mean particle size is calculated to be 41 ± 8 nm.

Powder X-ray diffraction (XRD) patterns of $Zn_xNi_{1-x}Fe_2O_4$ ($x = 0$, 0.2, 0.4, 0.6, 0.8, 1) obtained at room temperature are shown in **Figure 3**a. All the XRD patterns confirm that the main crystalline phase is the spinel crystal phase for $Zn_xNi_{1-x}Fe_2O_4$ nanomaterials. It is worth noting that, for $x = 0$ and $x = 1$, the experimental patterns fully match with the inverse spinel Trevorite[40] ($NiFe_2O_4$, ref. code 01-086-2267, ICSD-040040 (ICSD release 1997)) and the normal spinel Franklinite[41] ($ZnFe_2O_4$, ref. code 01-074-2397, ICSD-028511 (ICSD release 1997)), respectively. For the intermediate compositions, with the increase of Ni content, there is a gradual shift of the peaks

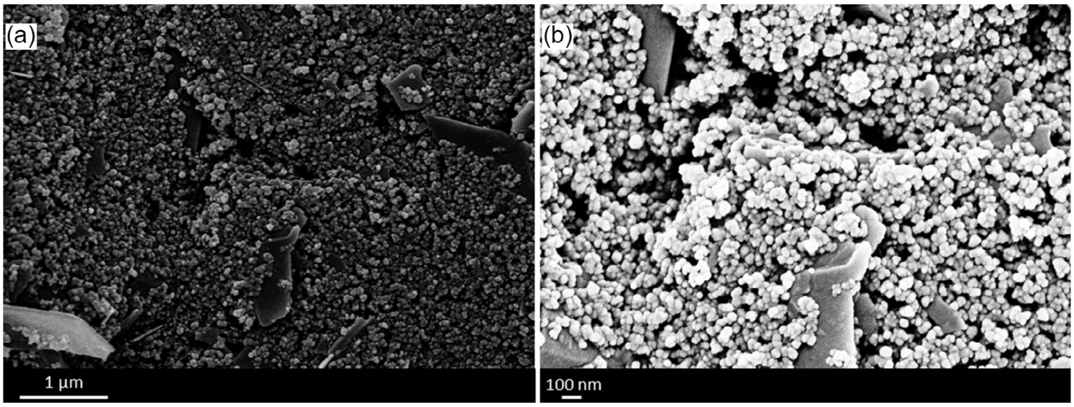

Figure 2. FE-SEM images of the surface of $ZnFe_2O_4$-modified WE at a) 50 kx and b) 250 kx magnification.

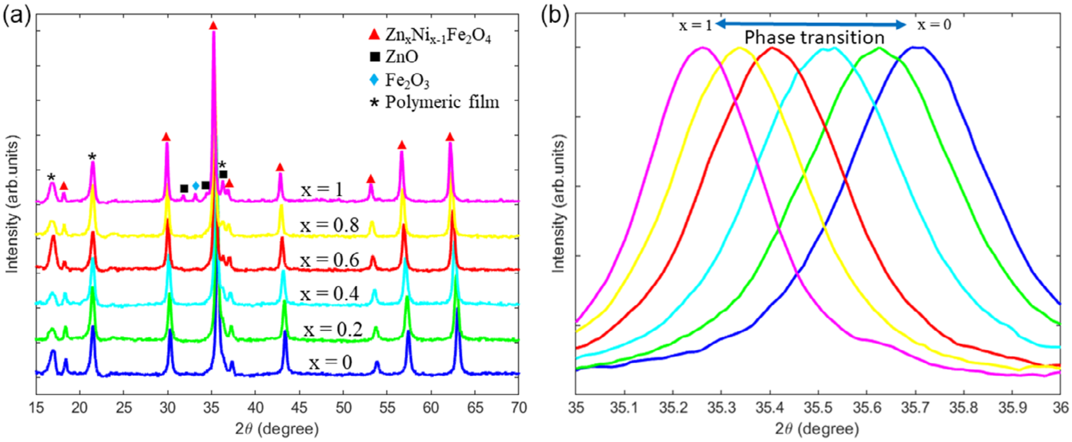

Figure 3. a) XRD patterns of $Zn_xNi_{1-x}Fe_2O_4$ nanomaterials; b) phase transition from normal to inverse spinel crystal structure.

toward higher angles in 2θ; Figure 3b shows, as an example, this shift for the most intense peak of the spinel. This shift in peaks suggests the gradual lattice volume expansion attributed to the fact that Ni(II) has a smaller ionic radius (69 pm) compared to the Zn(II) ionic radius (74 pm).[42] The same shifting behavior in XRD was also reported in the literature where Co(II) was substituted by Ni(II) in the lattice of $CoFe_2O_4$ as the crystal structure changed from normal spinel to inverse spinel.[43] This gradual shift confirms that the synthesized materials have a crystal structure transiting between the normal and inverse spinel as expected. However, all these crystal structures belong to the cubic Fd-3m space group.

In addition to the $Zn_xNi_{1-x}Fe_2O_4$ spinel phase, all the XRD patterns show the presence of three peaks at 2θ values of 16.8°, 21.4°, and 36.3°; the last peak, for spectra characterized by low Zn content ($x = 0$, 0.2, 0.4), is partially overlapped to the main peak of the spinel, and it becomes evident for higher Zn content ($x = 0.6$, 0.8, and 1) because of the shift of the main peak to lower angles. A polymeric sealing was used during the XRD analysis as a safety measure (because of the nanometric dimension of the spinel powders). To check the source of these three unknown peaks, XRD with and without the polymeric sealing was recorded. The three abovementioned peaks were not found in the diffractogram of the selected unsealed sample as shown in Figure S1, Supporting Information, while they were found for the sealed samples as discussed above. Therefore, those three peaks are assigned to the presence of the polymeric film.

Besides, the XRD pattern of $ZnFe_2O_4$ ($x = 1$) shows four low-intensity peaks between 30° and 36°. The position of these peaks is compatible with that of the most intense peaks of ZnO and Fe_2O_3, respectively; the presence of these oxides in the material could be justified by the synthesis process adopted.

The average crystallite size of the particles was calculated using both Scherrer's method and Williamson–Hall's method (see Equation (S1)–(S4), Supporting Information). The crystallite sizes obtained by the two different methods are consistent. As reported in **Table 2**, the average crystallite size varies between 24 and 35 nm which is very well in agreement with the particle size estimated from FESEM analysis. The crystallite size varies irregularly from material to material due to the type of synthesis procedure used. Autocombustion synthesis does not allow precise control over the growth of the crystallites. A similar irregular variation of crystallite sizes was observed in a previous work[4] where the authors used autocombustion as a synthesis procedure. The addition of Zn into the inverse spinel of $NiFe_2O_4$ did not show much effect on the crystallite size may be due to the similar ionic radii of 69 and 74 pm for Ni(II) and Zn(II), respectively.[42]

Table 2. The average crystallite size of $Zn_xNi_{1-x}Fe_2O_4$ nanomaterials.

Material	*D* Scherrer [nm]	*D* WH [nm]
$NiFe_2O_4$	26.6	28.3
$Ni_{0.8}Zn_{0.2}Fe_2O_4$	23.6	24.3
$Ni_{0.6}Zn_{0.4}Fe_2O_4$	24.2	22.7
$Ni_{0.4}Zn_{0.6}Fe_2O_4$	26.8	26.6
$Ni_{0.2}Zn_{0.8}Fe_2O_4$	28.4	27.1
$ZnFe_2O_4$	35.2	28.9

2.1.2. Spectroscopic Characterization

Pure/mixed ferrites crystallize in a spinel structure of space group Fd-3m with five active Raman bands ($A_{1g} + E_g + 3T_{2g}$) as predicted by group theory.[44–47] A well-known (inverse) spinel structure is a magnetite (Fe_3O_4) structure where "Td" and "Oh" sites are occupied by Fe ions whereas in $NiFe_2O_4$, half of Fe ions occupy the "Td" sites, and the "Oh" sites are shared between Ni and Fe ions. This suggests uniform bond distances between Fe and O in Fe_3O_4 but a bit of distortion in bond distances is possible in $NiFe_2O_4$ due to the difference in ionic radii of Ni and Fe ions. In simple words, a disturbance in the local structure can be observed as Raman spectroscopy is very sensitive to local structural changes. This suggests that we can observe the same or similar structural changes in $Zn_xNi_{1-x}Fe_2O_4$ nanomaterials as we change the composition of the material from $x = 0$ to 1. Raman spectra of all six materials are shown in **Figure 4**a. The changes in the spectra can be clearly observed as we change the composition of the material due to local changes in the crystal structure. The spectra are matching very well with the spectra of Fe_3O_4 reported in the literature;[47] the main difference is that the bands of Fe_3O_4 are sharp and very well defined while in Zn–Ni mixed ferrites we observe a shoulder or doublet-like (with two cations) and triplet-like (with three cations) behavior in Raman bands: as the ionic radius varies so does the bond distance.

For the inverse spinel $NiFe_2O_4$, the five Raman peaks are observed at 703 (A_{1g} band), 573 ($T_{2g}(3)$ band), 482 ($T_{2g}(2)$ band), 333 (E_g band), and 211 ($T_{2g}(1)$ band) cm^{-1}. Fe-related A_{1g} mode is observed at 703 cm^{-1}; after inserting Ni into the ferrite structure an additional strong mode is observed at 668 ± 10 cm^{-1} which is assigned to Ni-related A_{1g} mode similar to what occurs for $MnFe_2O_4$[45] and the peaks are very close to the peaks reported in the literature.[43,47] As we take the spectrum of $Ni_{0.6}Zn_{0.4}Fe_2O_4$ apart from the peaks related to Fe and Ni at 698 and 667 cm^{-1}, we observe another strong peak at 644 cm^{-1} due to the presence of Zn within the A_{1g} band which is assigned to Zn–O vibrations at "Td" sites as mentioned in the past.[48,49] Similarly, for the normal spinel $ZnFe_2O_4$, the Fe-related peak at 646 and Zn-related peak at 612 cm^{-1} within the A_{1g} band have been assigned as shown in Figure 4b. Apart from the five usual Raman bands, an extra band indicated as "*" around 400 cm^{-1} is assigned to an unknown band from spinel ferrites. The peak positions of the other four Raman bands $T_{2g}(3)$, $T_{2g}(2)$, E_g, and $T_{2g}(1)$ have been assigned in the Raman spectra and the positions are reported for the selected materials in **Table 3**.

The Kubelka–Munk function $F(R_\infty)$ of diffuse reflectance (DR) UV–vis spectra of powder samples is reported in **Figure 5**. $F(R_\infty)$ is described as Equation (1)

$$F(R_\infty) = \frac{(1 - R_\infty)^2}{2R_\infty} = \frac{K}{s} \tag{1}$$

where R_∞ is the fraction of incident UV–vis light that is remitted by the layer considered as an infinitely thick sample, s is the scattering coefficient, and K is the molar absorption coefficient.[50]

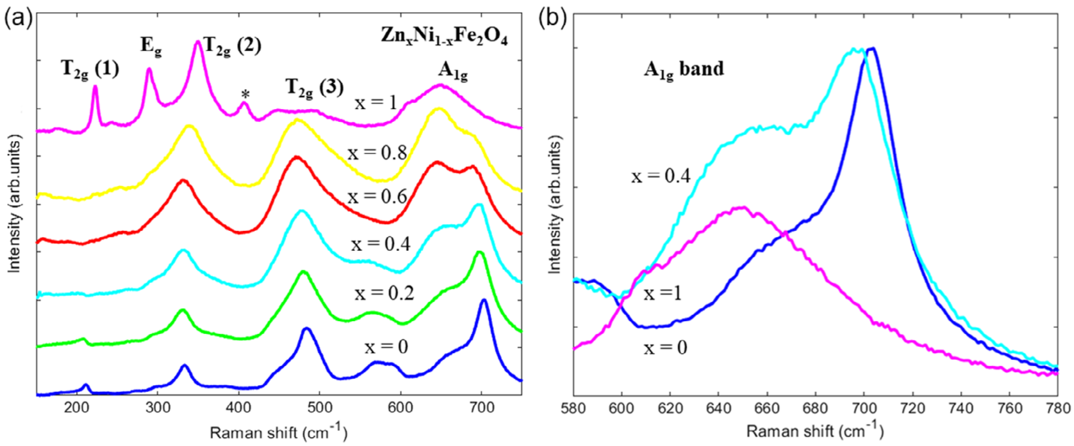

Figure 4. a) Raman spectra of $Zn_xNi_{1-x}Fe_2O_4$ nanomaterials; b) intensive A_{1g} Raman band showing the doublet- and triplet-like bands of $NiFe_2O_4$ ($x = 0$), $Ni_{0.6}Zn_{0.4}Fe_2O_4$ ($x = 0.4$), and $ZnFe_2O_4$ ($x = 1$), respectively (* unknown Raman band).

Table 3. Raman modes from the Raman spectra of $Zn_xNi_{1-x}Fe_2O_4$ ($x = 0$, 1).

	Raman modes [cm^{-1}]			
Mode	$ZnFe_2O_4$[48]	$NiFe_2O_4$[47]	$ZnFe_2O_4$	$NiFe_2O_4$
A_{1g} – Fe	647	681	646	703
Ni	–	–	–	668
Zn	–	–	612	–
$T_{2g}(3)$	451	555	450	573
$T_{2g}(2)$	355	472	349	482
E_g	246	312	289	333
$T_{1g}(1)$	221	197	224	211

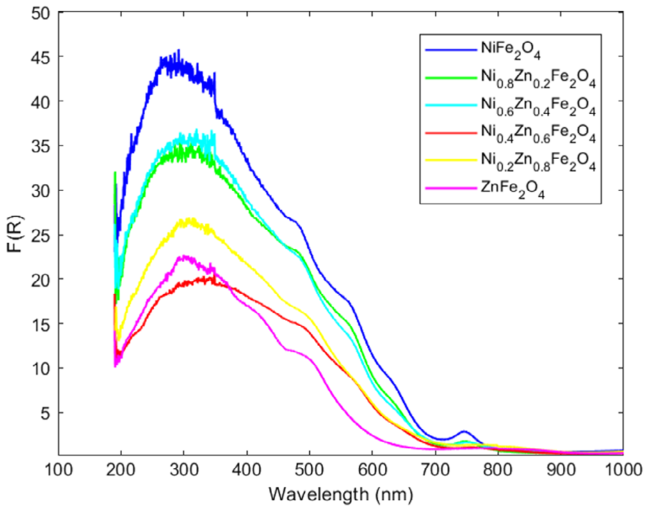

Figure 5. DR UV–vis spectra of $Zn_xNi_{1-x}Fe_2O_4$ nanomaterials.

$Zn_xNi_{1-x}Fe_2O_4$ nanomaterials show different Kubelka–Munk curves as reported in Figure 5. The spectra show a different onset of absorption and different bands, likely related to localized electronic levels. Nickel ferrite shows four bands at 485, 560, 635, and 750 nm. The whole set of bands is assigned to electronic transitions of Ni(II) ions in the spinel structure with octahedral and tetrahedral coordination geometries. Following the literature,[51] we assigned the bands at 485 and 571 nm to $^3A_{2g}(F) \rightarrow {}^3T_{2g}(F)$ transitions of octahedral Ni(II) ions, whereas the bands at 635 and 750 nm are assigned to $^3T_1(F) \rightarrow {}^3T_{1g}(P)$ transition of tetrahedrally coordinated Ni(II) ions[52] and the $^3A_2(F) \rightarrow {}^3T_1(F)$ transitions as the *d–d* transition of Ni(II) ions in a tetrahedral environment.[53] This is evident from the fact that Ni ferrite is an inverse spinel material with Ni(II) sharing the octahedral and tetrahedral sites with Fe(III).[24,25]

Zn ferrite shows a main shoulder at 500 nm assigned to a CF transition $^6A_2 \rightarrow {}^4A_1(G)$ of octahedral Fe(III).[54] The same Fe(III) coordination geometry is supported by the occurrence of a broad band at 800 nm, assigned to $^6A_2 \rightarrow {}^4T_1(G)$ in the octahedral Fe(III).[55] It is typical of a normal spinel where Fe(III) sits in octahedral sites.[24,25] The Zn–Ni mixed ferrites show the same bands with highly intense Ni(II) related bands at higher Ni content ($Zn_{0.2}Ni_{0.8}Fe_2O_4$ and $Zn_{0.4}Ni_{0.6}Fe_2O_4$), while $Zn_{0.6}Ni_{0.4}Fe_2O_4$ and $Zn_{0.8}Ni_{0.2}Fe_2O_4$ (at higher Zn content) mainly showed Zn ferrite-related bands as reported in Figure 5.

The energy gap (E_g) of the materials is estimated by Tauc's plot[56] as shown in **Figure 6**. Direct transitions were considered, and the evaluated energy gap of nanomaterials is reported in **Table 4**. The estimated E_g of $NiFe_2O_4$ (2.47 eV) and $ZnFe_2O_4$ (2.52 eV) is very close to the E_g values reported previously.[17,57–59] Addition of Zn to $NiFe_2O_4$ lattice brings about a change in the nanomaterials' energy gap. Figure 5 shows that $Zn_xNi_{1-x}Fe_2O_4$ nanomaterials have different absorption spectra in terms of both onset of absorption and of other spectroscopic features ascribable to surface electronic sites. Concerning the corresponding bandgap energy values (Table 4), it was impossible to find a regular trend with the nanoparticles size. The reported XRD and FESEM analyses allowed us to determine the nanomaterials' crystallites and particles size, respectively. The former is around 30 nm, and the latter around 50 nm, but both types of values are affected by some uncertainty/

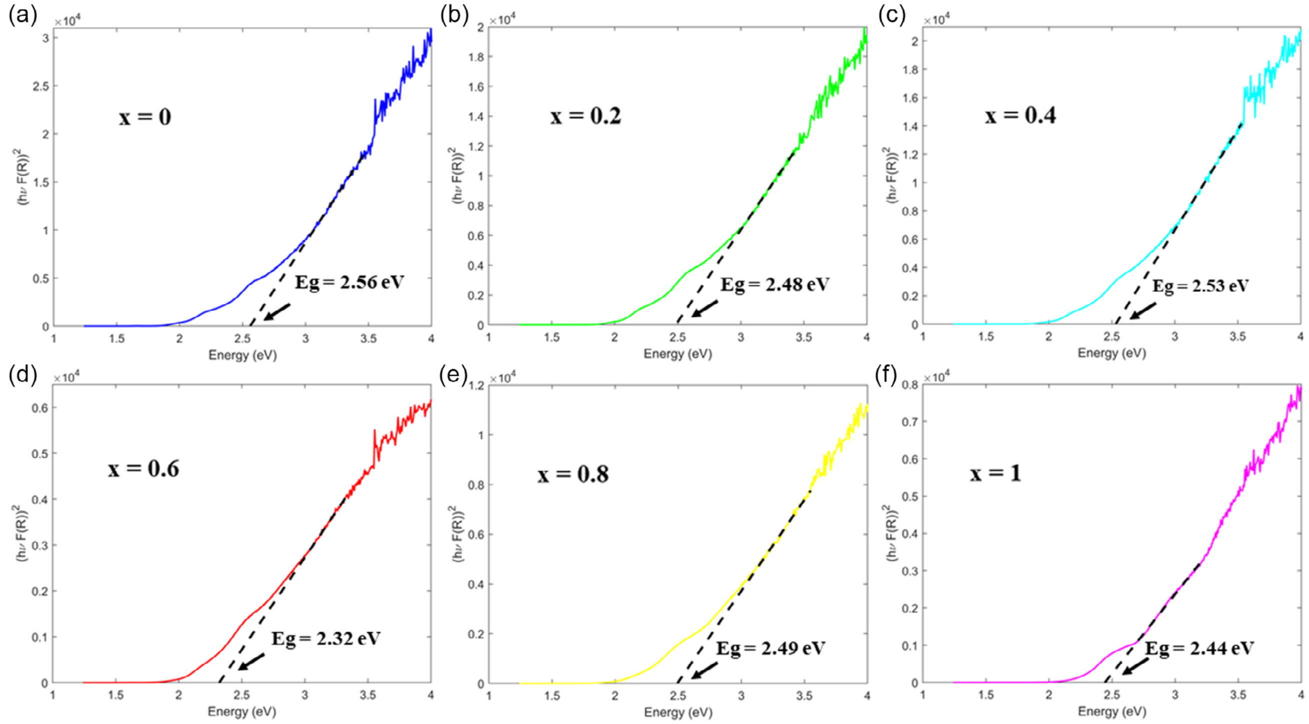

Figure 6. a–f) Tauc plots with linear fit extrapolated to the *x*-axis to determine the energy bandgap of $Zn_xNi_{1-x}Fe_2O_4$ ($x = 0$, 0.2, 0.4, 0.6, 0.8, 1) nanomaterials, respectively.

Table 4. E_g, E_v, and E_c of $Zn_xNi_{1-x}Fe_2O_4$ nanoparticles.

Material	E_g [eV]	E_v [eV]	E_c [eV]
$NiFe_2O_4$	2.56	−0.56	2.00
$Ni_{0.8}Zn_{0.2}Fe_2O_4$	2.48	−0.64	1.84
$Ni_{0.6}Zn_{0.4}Fe_2O_4$	2.53	−0.87	1.66
$Ni_{0.4}Zn_{0.6}Fe_2O_4$	2.32	−0.66	1.66
$Ni_{0.2}Zn_{0.8}Fe_2O_4$	2.49	−1.35	1.14
$ZnFe_2O_4$	2.44	−1.73	0.71

error. It is generally acknowledged that nanoparticles' size and shape play crucial roles in determining the electronic levels energy in a material.[60–64] Concerning the shape, it can significantly affect the light absorption leading to different band gap energies.[61,63,64] In our discussion, we assumed for sake of simplicity that the shape of nanoparticles is spherical but a closer look into the SEM images shows some irregular shapes in the different nanomaterials reported in this work. Due to irregular variations in (crystallite and) particle sizes, slight variations in particle shape may lead to an irregular variation in the bandgap energy, as it was not possible to find a smooth relationship between the nanoparticles size and the calculated bandgap values of the studied nanomaterials. Moreover, it has to be remarked that the DR UV–vis spectra in Figure 5 show the occurrence of surface energy levels, which may strongly affect the calculation of the bandgap. Such surface energy levels can be related to the presence of surface states/defects which can be responsible for the observed tailing in spectra, finally hampering a more accurate calculation of the nanomaterials' bandgap.[64]

The elemental composition and oxidation states of the elements were examined by X-ray photoelectron spectroscopy (XPS). The full survey scan spectra reported in Figure S2, Supporting Information, show the peaks corresponding to Ni, Zn, Fe, and O, which are present in the composition of the $Zn_xNi_{1-x}Fe_2O_4$ nanomaterials, and adventitious C. Core-level high-resolution (HR) spectra of Fe 2*p*, Ni 2*p*, Zn $2p_{3/2}$, and O 1*s* were recorded, and fitting was performed, as shown in **Figure 7**. The binding energies of Zn, Ni, Fe, and O in the composition of $Zn_xNi_{1-x}Fe_2O_4$ nanomaterials are listed in Table S1, Supporting Information. Fe 2*p* spectral regions include two main peaks located at 711–710 eV (Fe $2p_{3/2}$) and 724.5–723.5 eV (Fe $2p_{1/2}$), with two broad shake-up peaks at higher binding energies related to Fe(III).[59,65,66] HR spectra of Ni 2*p* show two main peaks located at ≈854.7 and ≈872.2 eV, which correspond to Ni $2p_{3/2}$ and Ni $2p_{1/2}$ peaks, respectively.[67,68] The two additional satellite features at higher binding energies are shake-up peaks characteristic of Ni(II) species.[69] HR spectra of Zn $2p_{3/2}$ show main peaks located at 1021.1–1021.4 eV related to Zn(II).[59,65,66] O 1*s* spectra were deconvoluted with two main components located at ≈529.7 and ≈531.4 eV, corresponding to O^{2-} in the lattice and O^{2-} in the hydroxyl group, respectively, while the additional shoulder at binding energy higher than 532 eV is due to adsorbed water.[69,70] XPS confirmed the valence states of Zn, Ni, Fe, and O as "+2", "+2", "+3", and "−2", respectively, in the composition of $Zn_xNi_{1-x}Fe_2O_4$ nanomaterials.

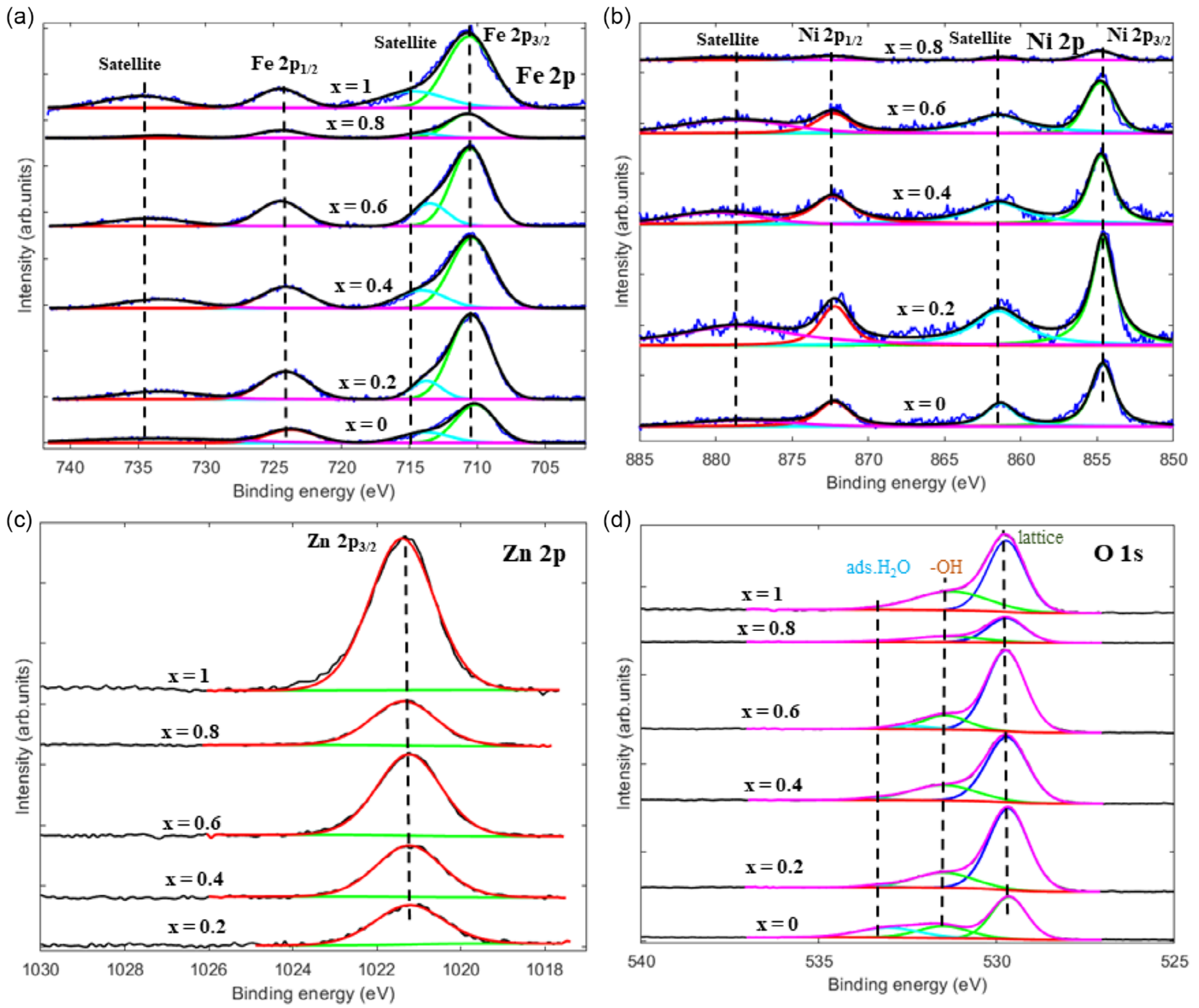

Figure 7. XPS high-resolution spectra of $Zn_xNi_{1-x}Fe_2O_4$ nanomaterials showing a) Fe 2*p*, b) Ni 2*p*, c) Zn 2*p*, and d) O 1*s*, respectively.

XPS valence band spectra of the nanomaterials are used to predict the valence band maximum of each material following the reported method.[71] The rising edge of the peak present in the XPS valence band spectra is extrapolated to the baseline of the flat XPS valence band spectra as shown in **Figure 8**, and the intercept of the baseline is reported as the maximum of the valence band (E_v). Fermi energy level (E_f) is assumed to be at zero eV, hence E_v is reported in negative energy values in Table 4. By summing the energy gap (E_g) to the energy of the valence band edge (E_v), we obtain the energy value (E_c) of the minimum of the conduction band. E_g, E_c, and E_v values for $Zn_xNi_{1-x}Fe_2O_4$ nanomaterials are reported in Table 4.

2.2. Electrochemical Characterization

CV was used to study the behavior of newly developed electrochemical sensors modified with $Zn_xNi_{1-x}Fe_2O_4$ nanoparticles. Figure S3a, Supporting Information, shows the CV curve for $NiFe_2O_4$ nanoparticles in methanol-modified sensor. We observe an improvement in oxidation current and potential compared to the bare sensor. To study the effect of the amount of nanoparticles deposition on the surface, the WE surface was modified by spreading 2, 5, 7, and 10 μL solutions of $NiFe_2O_4$; the corresponding cyclic voltammograms are shown in Figure S3b, Supporting Information. As we increased the amount of deposition from 2 to 5 μL the performance improved but when we moved from 5 to 7 and then to 10 μL the oxidation peak current reduced significantly. This explains that a higher amount of deposition on the surface of WE leads to higher resistance, thus lower activity. After this preliminary observation, 5 μL was chosen as the standard amount of deposition to study further the performance of the sensors.[72]

Figure 9a shows the cyclic voltammograms of $NiFe_2O_4$ (from here on nanoparticles are dispersed in butanol) and bare sensors with and without 1 mM PCA in 0.1 M PBS pH 6.9 at a scan rate (ν) of 100 mV s^{-1}. It is noticed that with the $NiFe_2O_4$ sensor, there are no redox peaks without PCA and clear redox peaks when PCA is present. This proves that the redox peaks are

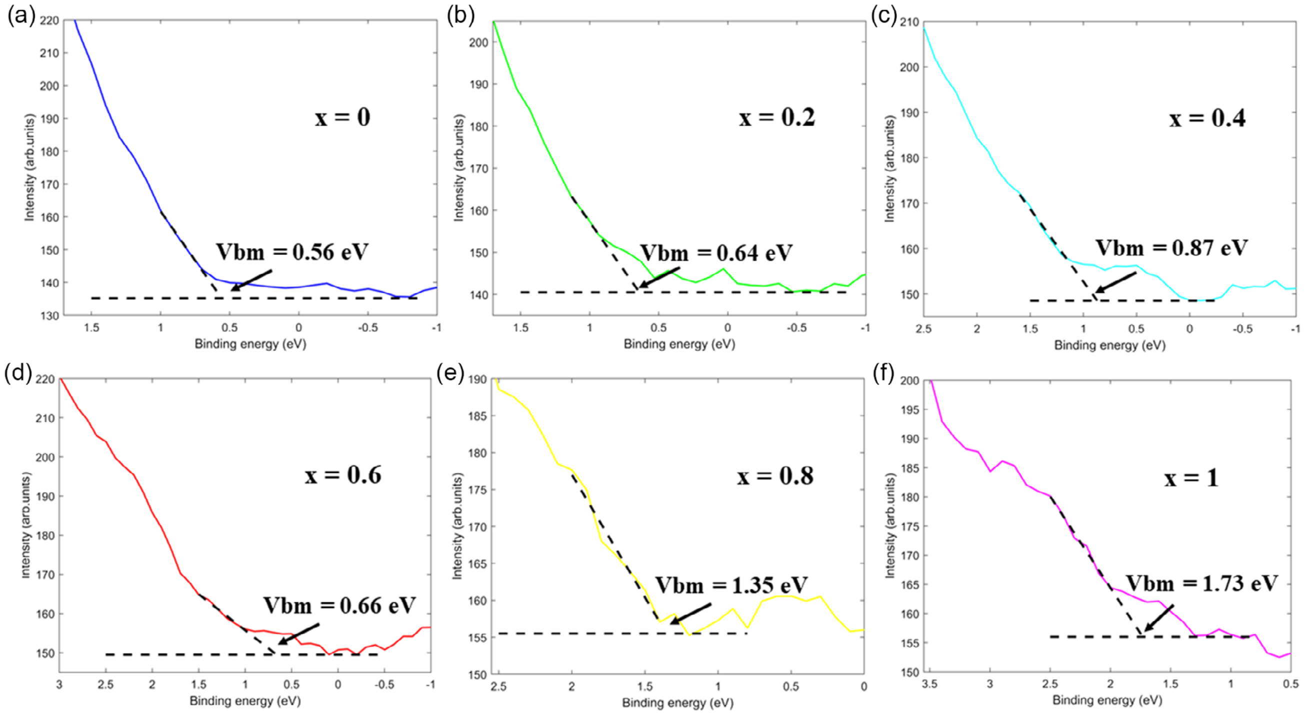

Figure 8. a-f) Valence band XPS spectra of $Zn_xNi_{1-x}Fe_2O_4$ nanomaterials, estimation of the valence band maximum of each material ($x = 0$, 0.2, 0.4, 0.6, 0.8, 1), respectively.

generated by the redox mechanism of PCA at the $NiFe_2O_4$ and electrolyte interface. When we compare the CV of bare (black curve) and $NiFe_2O_4$ (blue curve) sensors, the performance of the $NiFe_2O_4$ sensor is better than the bare sensor with an oxidation peak current of 40.40 ± 0.23 μA (from here on all the errors reported as standard error mean (sem)) at a potential of 282 ± 1 mV while the bare sensor has an oxidation peak current of 34.5 ± 0.2 μA at a potential of 396 ± 2 mV. Figure 9b shows the cyclic voltammogram of the $ZnFe_2O_4$ (magenta curve) sensor with an oxidation peak current of 52.14 ± 0.56 μA at a potential of 244 ± 1 mV. This means a current improvement of 6 μA and a reduction in the potential of 114 mV for the $NiFe_2O_4$ sensor and 18 μA and a reduction in the potential of 152 mV for the $ZnFe_2O_4$ sensor, respectively, compared to the bare sensor. Figure 9c shows the comparison of cyclic voltammograms of $Zn_xNi_{1-x}Fe_2O_4$ ($x = 0$, 0.2, 0.4, 0.6, 0.8, 1) and bare sensors. **Table 5** shows that all $Zn_xNi_{1-x}Fe_2O_4$ sensors have improved performance in terms of oxidation current and potential compared to the bare sensor with the $ZnFe_2O_4$ one being the sensor with the best performance. As the % of Zn increases in $Zn_xNi_{1-x}Fe_2O_4$ ($x = 0$, 0.2, 0.4, 0.6, 0.8, 1), the oxidation current increased gradually due to the transition from inverse spinel to the normal spinel. The conductivity of $NiFe_2O_4$ is lower than that of $ZnFe_2O_4$,[17] due to the occupancy of Ni and Zn in "Oh" and "Td" sites, respectively, in the inverse and normal spinel structure. The addition of Zn is slowly changing the crystal structure from inverse to normal spinel (as shown by XRD) and so does the conductivity of the material. This explains the increase in the oxidation current as we increased the Zn% in the composition of $Zn_xNi_{1-x}Fe_2O_4$.

Table 5 shows the effect on the potential and the current of the oxidation peak. The oxidation peak of PCA is located at 396 ± 2 mV on the bare sensor. However, the peaks shifted to lower potentials when the Zn–Ni ferrites were immobilized onto the SPCE surface. The oxidation peaks are now located at 282 ± 2 mV for $NiFe_2O_4$ and at 244 ± 1 mV for $ZnFe_2O_4$, respectively, for a 1 mM PCA solution. We observe a maximum of 152 mV by using $ZnFe_2O_4$ nanoparticles which is a very effective saving in energy. This leads to less energy in ET, meaning that the proper electronics design requires less voltage in driving the ECI. This is clear evidence of the well-known Nernst effect (Equation (S5) and (S6), Supporting Information) due to the presence of nanostructured layers at the interface helping to move the redox peaks toward lower potentials.[73–75]

CV was conducted by varying the scan rate "ν" from 50 to 300 mV s^{-1} (step of 50 mV s^{-1}). Figure 9d–f shows the cyclic voltammograms of bare, $NiFe_2O_4$, and $ZnFe_2O_4$ sensors, respectively, while the inset plots show the variation of redox currents with respect to $\sqrt{\nu}$. It is noticed that the peak positions are shifting with "ν" and the oxidation current (I_{pa}) and reduction current (I_{pc}) are varying linearly with $\sqrt{\nu}$ with linear regression equations and regression coefficients reported in **Table 6**. The other $Zn_xNi_{1-x}Fe_2O_4$ ($x = 0.2$, 0.4, 0.6, 0.8) sensors have similar behaviors as reported in Figure S4, Supporting Information, while their linear regression equations are reported in Table S2, Supporting Information.

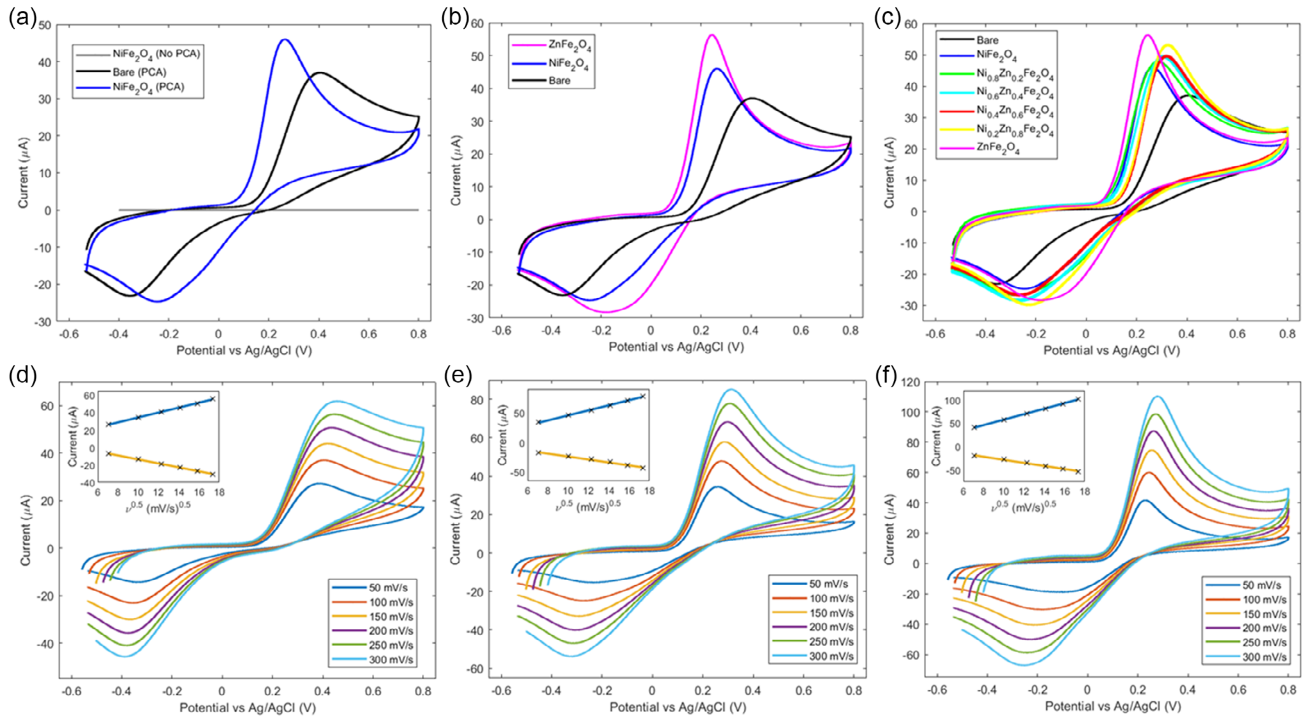

Figure 9. a) Cyclic voltammograms of NiFe$_2$O$_4$ and bare sensors without (only PBS), and with 1 mM paracetamol in 0.1 M PBS pH 6.9 at a scan rate of 100 mV s^{-1}. Comparison of cyclic voltammograms of b) ZnFe$_2$O$_4$, NiFe$_2$O$_4$, bare sensors, and c) Zn$_x$Ni$_{1-x}$Fe$_2$O$_4$ sensors with 1 mM paracetamol in 0.1 M PBS pH 6.9 at a scan rate of 100 mV s^{-1}. Cyclic voltammograms by varying the scan rate from 50 to 300 mV s^{-1} (step 50 mV s^{-1}) of d) bare, e) NiFe$_2$O$_4$, and f) ZnFe$_2$O$_4$ sensors. Inset: redox current versus $\sqrt{\nu}$.

Table 5. Oxidation peak current and potentials of the bare and the Zn$_x$Ni$_{1-x}$Fe$_2$O$_4$ sensors.

Sensor	Current [μA]	Potential [mV]
Bare	34.5 ± 0.2	396 ± 2
NiFe$_2$O$_4$	40.4 ± 0.2	282 ± 1
Ni$_{0.8}$Zn$_{0.2}$Fe$_2$O$_4$	43.2 ± 0.5	288 ± 3
Ni$_{0.6}$Zn$_{0.4}$Fe$_2$O$_4$	46.4 ± 0.3	306 ± 3
Ni$_{0.4}$Zn$_{0.6}$Fe$_2$O$_4$	47.8 ± 0.9	317 ± 3
Ni$_{0.2}$Zn$_{0.8}$Fe$_2$O$_4$	49.7 ± 1.0	322 ± 2
ZnFe$_2$O$_4$	52.4 ± 0.6	244 ± 1

Table 6. I_{pa}, I_{pc} regression equations of the bare and the Zn$_x$Ni$_{1-x}$Fe$_2$O$_4$ ($x = 0, 1$) sensors.

Sensor	I_{pa}	R^2	I_{pc}	R^2
Bare	$2.82\sqrt{\nu} + 6.35$	0.998	$-2.26\sqrt{\nu} + 8.93$	0.999
NiFe$_2$O$_4$	$4.25\sqrt{\nu} + 3.17$	0.997	$-2.47\sqrt{\nu} + 0.83$	0.987
ZnFe$_2$O$_4$	$5.86\sqrt{\nu} + 0.87$	0.999	$-3.27\sqrt{\nu} + 4.35$	0.991

Another well-known effect from electrochemistry is that the maximum peak current collected due to the reaction at the ECI is directly related to the concentration (C) of the redox species through Randles–Sevčik equation (Equation (S7), Supporting Information).[73] As we increase "ν", "I" increases linearly with $\sqrt{\nu}$. Increasing "ν", the speed at which the potential applied to the sensor increases, resulting in a decrease in diffusion layer thickness (d) leading to higher currents by adding a capacitive current ($I_c = c\, dE/dt$; $\nu = dE/dt$; c = capacitance at the interface) to the faradaic current.[73,76] Our results clearly show this effect and the peak position changed with "ν"; these two concurring effects show that the electrochemical interface is a freely diffusing quasireversible one.[77]

Figure 10a–c shows that the redox peak positions E_{pa} (anodic peak position) and E_{pc} (cathodic peak position) are varying linearly with respect to $\ln(\nu)$ with linear regression equations in **Table 7** and Figure 10d–f shows that ΔE_p is varying linearly as a function of $\ln(\nu)$ with linear regression equations reported in **Table 8**. Figure S5, Supporting Information, shows the redox positions with $\ln(\nu)$ of Zn$_x$Ni$_{1-x}$Fe$_2$O$_4$ ($x = 0.2, 0.4, 0.6, 0.8$) sensors and Table S3, Supporting Information, reports the linear regression equations. Following this, another big advantage we have obtained is that all Zn$_x$Ni$_{1-x}$Fe$_2$O$_4$ sensors have a lower ΔE_p compared to bare carbon sensor which points toward a higher possibility of reversibility compared to the bare sensor. As the redox peak currents are varying linearly as a function of $\sqrt{\nu}$, and redox peak positions are varying linearly as a function of $\ln(\nu)$, we applied Laviron model[72,78] to calculate the electron transfer rate coefficient (α) and "k". In Laviron model, the cathodic and anodic peak potentials are described as Equation (2) and (3)

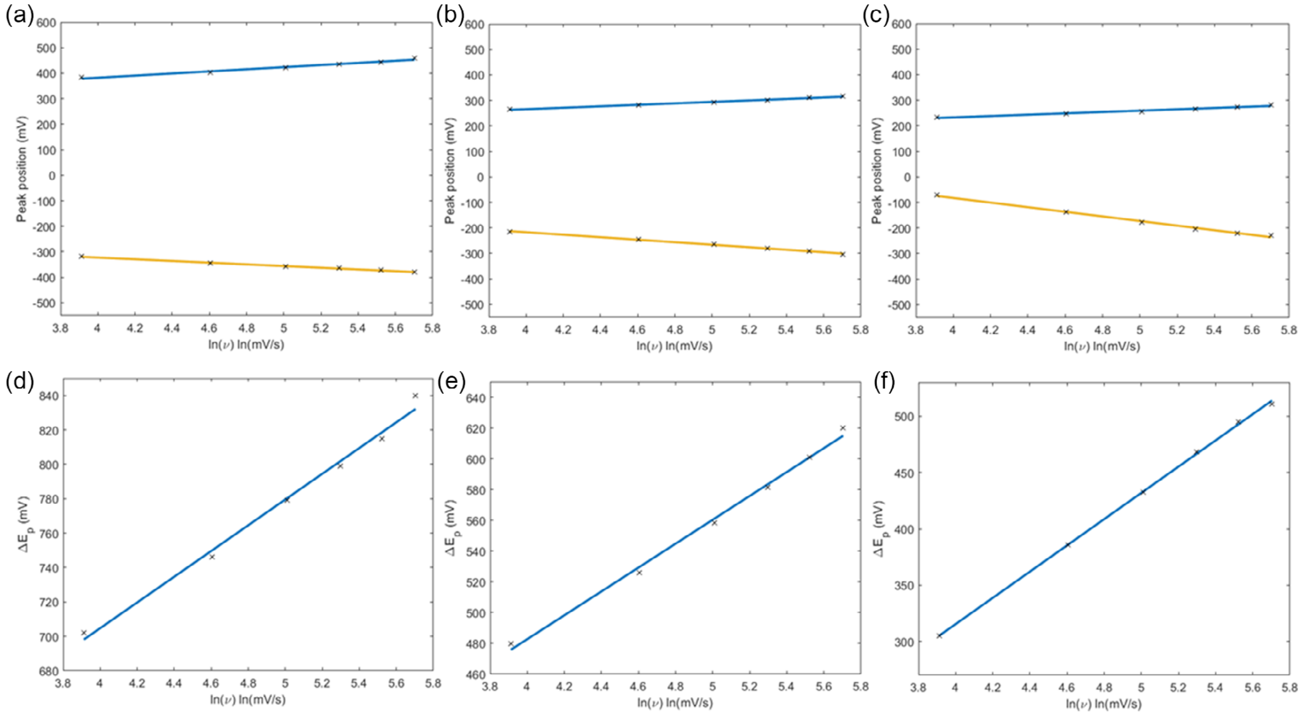

Figure 10. Plots of E_{pa} (blue), E_{pc} (green) with $\ln(\nu)$ for a) bare, b) $NiFe_2O_4$, and c) $ZnFe_2O_4$ sensors, respectively. ΔE_p as a function of $\ln(\nu)$ for d) bare, e) $NiFe_2O_4$, and f) $ZnFe_2O_4$ sensors, respectively.

Table 7. E_{pa}, E_{pc} regression equations for bare and $Zn_xNi_{1-x}Fe_2O_4$ ($x = 0, 1$) sensors.

Sensor	E_{pa}	R^2	E_{pc}	R^2
Bare	$41.49 \ln(\nu) + 216.14$	0.973	$-33.33 \ln(\nu) - 189.33$	0.996
$NiFe_2O_4$	$28.6 \ln(\nu) + 151.27$	0.989	$-49.04 \ln(\nu) - 20.86$	0.997
$ZnFe_2O_4$	$26.39 \ln(\nu) + 127.29$	0.975	$-90.212 \ln(\nu) - 278.3$	0.996

Table 8. ΔE_p regression equations for bare and $Zn_xNi_{1-x}Fe_2O_4$ ($x = 0, 1$) sensors.

Sensor	ΔE_p	R^2
Bare	$74.81 \ln(\nu) + 405.47$	0.991
$NiFe_2O_4$	$77.64 \ln(\nu) + 172.13$	0.995
$ZnFe_2O_4$	$116.64 \ln(\nu) - 151.01$	0.999

$$E_{pc} = E^0 - \left(\frac{RT}{\alpha nF}\right)\ln\left[\frac{\alpha}{|m|}\right] \tag{2}$$

$$E_{pa} = E^0 + \left(\frac{RT}{(1-\alpha)nF}\right)\ln\left[\frac{(1-\alpha)}{|m|}\right] \tag{3}$$

where $m = (RT/F)(k/n\nu)$, n is the number of electrons involved in the redox reaction, ν is the scan rate, E^0 is the surface standard potential, R is the universal gas constant, T is the absolute temperature in Kelvin, and F is the Faraday constant respectively. "α" was calculated by using the slopes of the plots E_{pa} and E_{pc} versus $\ln(\nu)$; we know that the redox process of paracetamol involves "2" electrons,[79] and ΔE_p was set at $\nu = 100\,\text{mV s}^{-1}$. "$k$" was calculated by substituting the known values into Equation (4)

$$\ln k = \alpha\ln(1-\alpha) + (1-\alpha)\ln\alpha - \ln\left(\frac{RT}{nF\nu}\right) - \alpha(1-\alpha)\frac{nF\Delta E_p}{\text{RT}} \tag{4}$$

Table 9 reports the values of α, k, and ΔE_p for all sensors. The bare sensor has a higher ΔE_p of 746 ± 5 mV and lower "k" $(2.22 \pm 0.19) \times 10^{-3}\,\text{ms}^{-1}$ while the $ZnFe_2O_4$ sensor has the lower ΔE_p of 386 ± 2 mV and higher "k" of $13.1 \pm 2.8\,\text{ms}^{-1}$. In **Figure 11**c, the points in red show the variation in "k" for

Table 9. α, k, and ΔE_p of bare and $Zn_xNi_{1-x}Fe_2O_4$ sensors.

Sensor	α	ΔE_p [mV]	k [ms^{-1}]
Bare	0.536 ± 0.004	746 ± 5	$(2.22 \pm 0.19) \times 10^{-3}$
$NiFe_2O_4$	0.367 ± 0.004	526 ± 6	0.27 ± 0.02
$Ni_{0.8}Zn_{0.2}Fe_2O_4$	0.333 ± 0.015	528 ± 4	0.39 ± 0.07
$Ni_{0.6}Zn_{0.4}Fe_2O_4$	0.296 ± 0.023	528 ± 7	0.62 ± 0.10
$Ni_{0.4}Zn_{0.6}Fe_2O_4$	0.340 ± 0.021	550 ± 6	0.25 ± 0.04
$Ni_{0.2}Zn_{0.8}Fe_2O_4$	0.391 ± 0.023	554 ± 8	0.14 ± 0.01
$ZnFe_2O_4$	0.226 ± 0.017	386 ± 2	13.1 ± 2.8

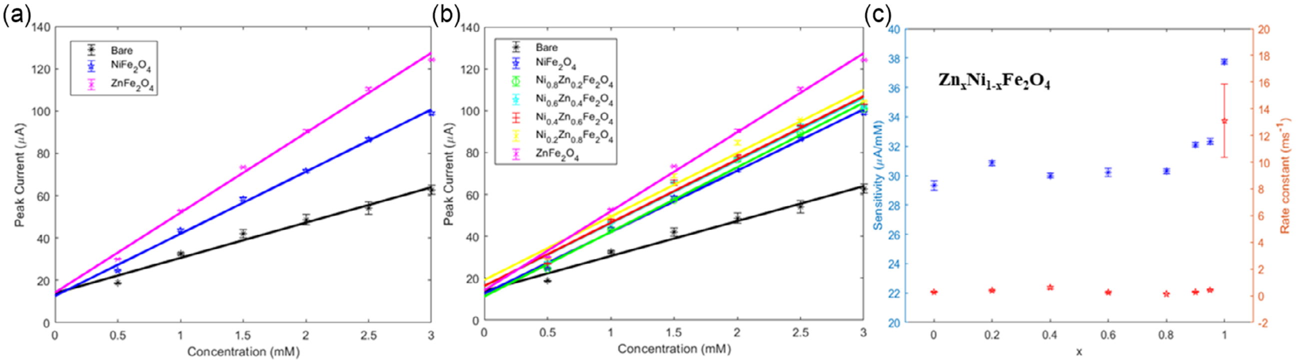

Figure 11. a,b) Comparison of calibration for bare, and $Zn_xNi_{1-x}Fe_2O_4$ sensors, c) sensitivity (*S*) and first-order kinetic rate constant (*k*) for $Zn_xNi_{1-x}Fe_2O_4$ sensors.

the $Zn_xNi_{1-x}Fe_2O_4$ sensors. From Randles–Sevčik's theory it was found that the electrochemical interface is not reversible, hence the redox positions differ with "ν" so does the ΔE_p.[73,77,80] Therefore, we have considered ΔE_p at a specific "ν" while calculating "*k*". All the $Zn_xNi_{1-x}Fe_2O_4$ sensors have a higher "*k*" with $ZnFe_2O_4$ being the best with a very high "*k*" compared to bare sensor giving rise to faster electrochemical reactions.[78]

Cyclic voltammograms were recorded 3 times for each type of sensor and oxidation peak currents were collected. The average of the three oxidation peak currents at each concentration of PCA "*C*" was taken to construct the calibration of the sensors by plotting the oxidation peak currents with respect to *C*. Figure 11a,b shows the calibration of bare and $Zn_xNi_{1-x}Fe_2O_4$ sensors; the slope of the calibration gave "*S*" toward PCA. LOD (the lowest detectable concentration of the analyte by a sensor) was calculated by using the sensitivity "*S*" and the standard deviation of the blank measurements (*D*) with the help of the equation $\text{LOD} = K\ D/S$,[81] where $K = 3$ as we target a 99.6% statistical confidence level. **Table 10** shows "*S*", R^2 of the calibration of the sensors, and the LOD of the bare and $Zn_xNi_{1-x}Fe_2O_4$ sensors. In Figure 11c, the blue points show the '*S*' trend for $Zn_xNi_{1-x}Fe_2O_4$ sensors. From Table 10, the bare sensor has a sensitivity of $16.68 \pm 0.93\ \mu\text{A mM}^{-1}$ with $R^2 = 0.975$ while $Zn_xNi_{1-x}Fe_2O_4$ sensors with $x = 0, 0.2, 0.4, 0.6, 0.8$ have a sensitivity close to $30\ \mu\text{A mM}^{-1}$, much higher than the bare one. $ZnFe_2O_4$ is the best sensor and has a sensitivity of $37.75 \pm 0.17\ \mu\text{A mM}^{-1}$ with $R^2 = 0.995$. Randles–Sevčik effect was observed in the oxidation current as we change "*C*" while constructing the calibration of the sensors.[82] This proves that the improvement in "*S*" is due to the nanostructured thin layers present at the ECI. The twofold improvement in "*S*" of the $ZnFe_2O_4$ sensor compared to the bare sensor is another very big achievement using ferrite nanomaterials.

Table 10. Sensitivity and limit of detection of bare and $Zn_xNi_{1-x}Fe_2O_4$ sensors.

Sensor	Sensitivity [μA mM^{-1}]	R^2	LOD [μM]
Bare	16.7 ± 0.9	0.975	3.26 ± 0.17
$NiFe_2O_4$	29.4 ± 0.4	0.996	6.93 ± 0.08
$Ni_{0.8}Zn_{0.2}Fe_2O_4$	30.9 ± 0.2	0.994	13.08 ± 0.05
$Ni_{0.6}Zn_{0.4}Fe_2O_4$	30.0 ± 0.2	0.986	16.41 ± 0.09
$Ni_{0.4}Zn_{0.6}Fe_2O_4$	30.2 ± 0.3	0.986	26.96 ± 0.24
$Ni_{0.2}Zn_{0.8}Fe_2O_4$	30.3 ± 0.2	0.976	42.94 ± 0.22
$ZnFe_2O_4$	37.8 ± 0.2	0.995	7.94 ± 0.04

Other important parameters when characterizing an electrochemical sensor are repeatability and reproducibility. Repeatability was checked by performing CV in the same conditions on the same sensor 5 times: relative standard error mean (R_{Sem}) of 0.57% and 1.07% for $NiFe_2O_4$ and $ZnFe_2O_4$ sensors, respectively, is observed. Reproducibility was checked by CV on three different sensors as reported in Figure S6, Supporting Information, and R_{Sem} of 1.84% and 1.58% is noticed for $NiFe_2O_4$ and $ZnFe_2O_4$ sensors, respectively.

3. Discussion

The surface/sides of the particles are not fully exposed to participate in the electrochemical reaction at the interface. Due to the aggregation of particles on the surface, each nanoparticle's contribution to the electrochemical sensing activity might not be the same because of the different reactivity of each particle participating in the electrochemical reaction. We observed a reduction in the oxidation current as we increased the thickness of the nanoparticles layer as this could have increased the aggregation of particles on the surface leading to a decreased reactivity of nanoparticles which affects the rate of electron transfer. We have achieved a similar shape of nanomaterials where the orientation of particles does not affect the electrochemical activity of nanoparticles which also allowed for direct comparison among the electrochemical performance of ferrite-based sensors.

As proved by XRD and Raman spectroscopy characterizations, $ZnFe_2O_4$ is a normal spinel material with Zn(II) sitting in tetrahedral sites and Fe(III) sitting in the octahedral sites. Alloying Ni(II) into $ZnFe_2O_4$ gradually modifies the normal spinel into an inverse spinel by removing Zn(II) from the crystal structure. In the inverse spinel, Ni(II) occupies the octahedral sites while Fe(III) ions are shared between the tetrahedral and octahedral sites. As shown by the electrochemical data, the performance of the sensors in terms of "*S*" and "*k*" gradually degrades as we increase the % of Ni(II) in the crystal structure. This can be understood by looking at the electronic transitions within the crystal structure of normal and inverse spinel. Investigation of the electronic properties of $NiFe_2O_4$ and $ZnFe_2O_4$ proved that the conductivity of the former is lower than that of the latter as the electron transfer is affected by the site occupancies and charge transfer between the cations.[17] The conduction in the spinel is explained by "small polaron-hopping" model, suggesting that the conduction is due to the charge transfer between cations in "Oh" sites of different valency electrons.[83] In ferrites, conduction is mainly due to Fe(III)/Fe(II) electron exchange in "Oh" site since varying the Fe ion concentration in "Oh" sites the conductivity changes. In inverse spinel, "Oh" sites are shared between Ni(II) and Fe(III) ions and the concentration of Fe(III) ions is increased when we decrease the % of Ni(II) by adding Zn(II) which has the tendency to occupy "Td" sites. When the crystal structure changes from inverse spinel to normal spinel, the concentration of Fe(III) in "Oh" sites increases, therefore the electron hopping mechanism between Fe(III) and Fe(II) in "Oh" sites increases; hence, the conductivity of normal spinel is higher compared to inverse spinel.[17] It has been widely reported in the literature that inverse spinel $NiFe_2O_4$ is a p-type semiconductor[43,84–87] due to hole hopping between intrinsic Ni(III)/Ni(II) while the normal spinel $ZnFe_2O_4$ is n-type[84,88–90] due to electron hopping of Fe(III)/Fe(II). It is well known that the p-type semiconductors are less conductive compared to the n-type semiconductors as the majority carriers are holes with a lower mobility than electrons. At low frequencies, inverse spinel has a higher dielectric constant compared to normal spinel. In general, dielectric materials are insulating or very low-conducting materials. Therefore, the dielectric property gives another hint on the conductivity of materials, high dielectric constant materials having a lower electrical conductivity than low dielectric constant materials.[43] Similar results were reported for the resistivity of ferrites, with higher resistivity (i.e., lower conductivity) for inverse spinel compared to normal spinel[86] due to the site occupancies of cations. All the above-mentioned properties of spinel materials justify the electrochemical behavior of $Zn_xNi_{1-x}Fe_2O_4$ sensors.

Using Burello and Worth's theoretical predictive model,[91,92] it is possible to understand the electron transfer mechanism from/to the biological molecules to/from the metal oxide nanoparticles. They described the electron transfer process by drawing relations between HOMO (highest occupied molecular orbital) and LUMO (lowest unoccupied molecular orbital) of biological molecules and E_c and E_v of metal oxide semiconductors. The prediction is that when the conduction band minimum of the metal oxide semiconductor is below or overlapping with the standard redox potential of the biological molecule the electron transfer is enhanced. However, this occurs only when one of the energy levels in the conduction band of the metal oxide semiconductor is matching in energy with one of the filled energy levels of the biological molecule.[92] This model assumed that there exist no surface states within the bandgap of the metal oxide semiconductor nanomaterials.[91,92] A similar approach has been used previously[93] to study the oxidative stress and toxic effects of 24 different metal oxides on biological molecules. The approach was a mix of experimental and theoretical models in mapping the E_c, E_v levels with the standard redox potentials of biological molecules.[93] Following such approaches,[91–93] we demonstrate the role of E_g, E_c, and E_v levels as critical semiconductor properties in electrochemical sensing applications. E_c represents the LUMO of metal oxide nanoparticles which participate in the electron transfers from/to the sensing material, while states sitting at energies below E_v (valence band) are occupied. If the oxidation potential E_{pa} of PCA is higher than the E_c of the ferrite nanomaterial, then direct electron tunneling can happen from PCA to the surface of the ferrite to the subsequent electron acceptors until the steady state is achieved in the system. A similar process occurs in the case of reduction where the reduction potential E_{pc} of PCA should be lower than the E_c of the ferrite material to allow the electrons to transfer to PCA from the surface of the nanomaterials.

Following this prediction, E_g from UV–vis spectroscopy, E_v from XPS, and E_c ($= E_g + E_v$) are used to draw the energy levels of ferrite nanoparticles. Experimentally obtained redox potentials E_{pa} and E_{pc} of PCA are marked to map the ferrites energy levels with redox potentials of PCA as shown in **Figure 12**. From Figure 12, only $ZnFe_2O_4$ E_c overlaps with the E_{pa} of PCA while materials with $x = 0–0.8$ have their E_c levels higher than the E_{pa} of PCA. This justifies the higher electrochemical performance of the $ZnFe_2O_4$ sensor for which we have recorded the lowest E_{pa} and the highest "S" and "k". It is reasonable that due to the overlap of $ZnFe_2O_4$ E_c and E_{pa} the sensor needs less energy for a favorable electron transfer from/to PCA. Therefore, the peak-to-peak separation ΔE_p is lesser leading to faster kinetics with a higher rate constant "k" and a high possibility of a reversible electrochemical reaction. We also notice a trend of the energy bands as we increase the % of Ni in $ZnFe_2O_4$; as E_c moves far from E_{pa} of PCA, the sensors require a higher voltage to provide electrons enough energy to make the direct electron transfer possible. This could be one of the reasons for the much lower "k" of sensors with Nickel compared to the $ZnFe_2O_4$ sensor. The

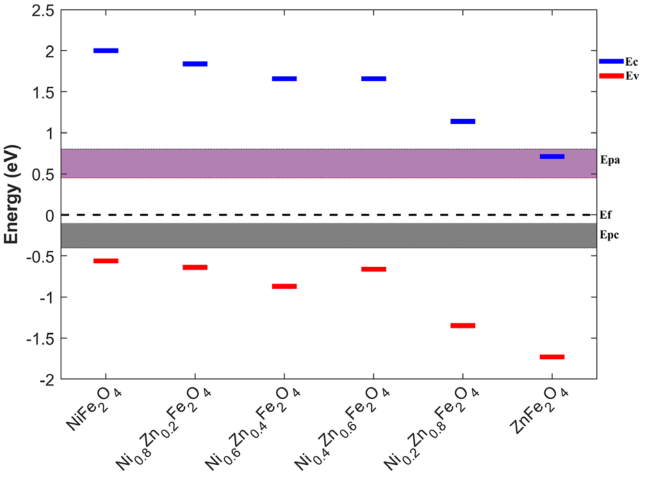

Figure 12. Conduction (E_c) band minimum (blue) and valence (E_v) (red) band maximum of $Zn_xNi_{1-x}Fe_2O_4$ nanomaterials constructed by using E_g (the energy gap between E_c and E_v) through UV–vis spectroscopy and valence band maximum from XPS technique. E_f is the Fermi-level energy. Electron transfer prediction from/to paracetamol to/from the surface of the WE by mapping the E_c of the WE with the experimental E_{pa} and E_{pc} of paracetamol.

sensitivity also decreased for sensors with $x = 0.8$ to 0 as the E_c level of nanomaterials has moved far from the E_{pa} level. In these cases, even though the E_c level is not below or overlapping with the E_{pa} the electron transfer has happened at the interface confirmed by the electrochemical results. This suggests that this predictive energy bands framework is not sufficient to explain the electron transfer in some cases.

Electron transfers are likely to occur when the orbitals from the semiconducting materials share an energy level with the orbital of the redox couples. We induce the orbitals of the nanomaterials to share energy levels with the molecular orbitals of the analyte molecules by applying a potential through a potentiostat. The amount of potential required to make this happen depends on how close the energy bands of the sensor materials are to the HOMO levels of the analyte. The closer the levels, the lesser potential it requires to make the electron transfer possible as it was the case for the $ZnFe_2O_4$ sensor. This process involves the acceptance of an electron that occupies an unoccupied energy level, while the donation process removes an electron from an occupied energy level. When the sensor is introduced into the analyte solution, the electron transfer happens at the ECI until chemical potential equilibrium occurs. This could be direct as in the case of the bare sensor where the electron transfer is between the carbon surface and PCA, while in ferrite-based sensors the transfer is two-stepped: from PCA to the ferrite nanomaterials and then to the carbon material (oxidation of PCA) or from carbon to ferrite nanomaterials to PCA (reduction of PCA). This is a very interesting approach as it allows us to describe the electron transfer phenomena at the ECI between the sensor surface and the analyte of interest.

DR UV–vis spectroscopy results point toward the presence of surface states from literature due to the presence of metal oxides (NiO, ZnO, Fe_2O_3) on the surface,[94,95] as confirmed by XRD spectra as shown in Figure 3. As electrochemical sensing is a surface phenomenon, we believe that the surface states play a crucial role in the electron transfer process. As reported in the literature, the surface states energy levels fall within the bandgap of the semiconducting materials[96] and from Figure 12 we know that the E_{pa} and E_{pc} levels are within the bandgap of ferrite nanomaterials. Hence, the surface state energy levels might be below or overlapping with the redox potentials of PCA so helping with the subsequent steps in electron transfer from/to PCA. This might explain what was observed in the cases of $x = 0$ to 0.8 where we have no overlap of E_c with E_{pa} but electron transfer was nevertheless observed, indicating that surface state levels could favor the electron transfer at the ECI. For example, in the oxidation of PCA, the full path of electrons will involve the transfer from the HOMO of PCA to the conduction band of ferrite nanomaterial, then to the surface state oxide, and finally to the LUMO of carbon material to achieve chemical potential equilibrium. Or electrons would transfer from the HOMO of PCA to the surface state energy level and then to the LUMO of carbon material to maintain the chemical potential equilibrium. Each step of the full path of the electron from PCA to carbon has its own "*k*" value. As the transfer steps occur in series, the overall "*k*" of the process is determined by the step with the lowest "*k*" value. Lower "*k*" values usually occur for tunneling processes while higher ones are obtained for direct transfer processes. This supports the higher "*k*" value of the $ZnFe_2O_4$ sensor where we have the overlap of E_c with E_{pa} with a high possibility of direct electron transfer. In the other cases with $x = 0–0.8$, we have no overlap of E_c with E_{pa} and lesser "*k*", indicating that the electron transfer could be through the energy barrier by tunneling.

Apart from ferrite surface state contribution to the electrochemical sensing, it is also important to consider the metal oxide dissolution in the environment. The dissolution depends on the metal solubility in the exposed environment and the difference in concentration (concentration gradient) of the nanoparticles' surface to the bulk solution phase.[97] For example, in the case of ZnO,[93] even though there was no overlap of E_c with the biological standard redox potentials, ZnO nanoparticles have shown toxic effects. These effects were reported[97–99] due to the dissolution of ZnO into Zn(II) and $Zn(OH)^+$ ions in water with moderate alkalinity and neutral pH.[90] The decrease in dissolution has reduced the toxic effects;[98] for less soluble materials the effects were due to both catalytic surfaces and ion release in the environment.[98,99] From the above causes and effects, to have a clear idea of electron transfer at ECI, it is required to have complete information about energy levels, surface state energy levels, and metal dissolution effects.

4. Conclusion

In this work, we demonstrate the electrochemical sensing activity of six $Zn_xNi_{1-x}Fe_2O_4$ ($x = 0$, 0.2, 0.4, 0.6, 0.8, 1) nanomaterials, their crystal structure transiting from spinel (cubic fcc) to inverse spinel (cubic fcc). In-house synthesis of the nanomaterials was performed through the autocombustion technique. FE-SEM and XRD confirmed that the synthesis was successful in producing nanomaterials with an average crystallite size of around 30 nm and particle size varying around 50 nm after depositing on the surface of the SPCE. XPS showed the correct elemental composition of the ferrite composites and confirmed the oxidation state of elements in the composites. Electrochemical sensing performance in detecting PCA in 0.1 M PBS at pH 6.9 was studied by CV. Sensitivity, kinetic rate constant, and LOD of sensors were evaluated and compared among six ferrite-based sensors and bare carbon sensors. It was found that the performance of the normal spinel sensor is the best in all electrochemical aspects compared to inverse spinel or mixed normal/inverse spinel sensors. Nevertheless, all the ferrite-based sensors had higher "*S*" and "*k*" values and hence were performing much better than the bare carbon sensor. We elucidated the electron transfer process at the electrochemical interface by mapping band edges of the metal oxide semiconducting materials with the redox potentials of PCA and highlighted the importance of the bandgap in the electron transfer process. The importance and role of surface energy levels were highlighted in the electron transfer process at the electrochemical interface. The issue of how metal oxide dissolution plays a role in affecting the electrochemical environment was also addressed. We found a very good agreement between electron transfer prediction using E_c and the main figures-of-merits in electrochemical sensing.

Electrochemical sensing performance is affected by many nanomaterial parameters such as size, crystallinity, specific surface area, active geometrical area of the electrode surface, amount of deposition, dissolution, the orientation of nanoparticles, semiconductor bandgap, and surface coating of nanoparticles. To make a direct comparison of electrochemical parameters among different sensors, the above material parameters should be the same for each material but achieving such a target is a rather challenging task. To further improve the performance of the above materials studied, it is possible to use other methods of synthesis to reduce particle aggregation and gain control over particle size. Surface coating of particles could help in stabilizing and reducing the agglomeration process while controlling the size through a bottom-up process. We are interested in further optimization of the ferrite nanomaterials to improve their performance and to test them for the detection of glucose, oxygen, and other biomolecules of interest.

5. Experimental Section

Chemicals: $Ni(NO_3)_2{\cdot}6H_2O$, $Zn(NO_3)_2{\cdot}6H_2O$, $Fe(NO_3)_3{\cdot}9H_2O$, $C(NH_2)_2O$ (Urea), NaH_2PO_4, Na_2HPO_4, $C_4H_{10}O$ (butanol), and paracetamol powder were purchased from Sigma–Aldrich and used without further modification.

Material Synthesis: **Scheme 1** presents the simple, cost-effective, single-step autocombustion synthesis method of ferrite nanomaterials adopted from the literature[12] without the need of any solvent. $Ni(NO_3)_2{\cdot}6H_2O$, $Zn(NO_3)_2{\cdot}6H_2O$, $Fe(NO_3)_3{\cdot}9H_2O$ were used as oxidizing agents, and $C(NH_2)_2O$ (urea) as a reducing agent. A redox mixture (1:1 mole ratio) was prepared in a crucible, kept inside a graphite reactor, and heated up to 600 °C within a furnace. Upon complete combustion, the final product was annealed at 600 °C for 1 h, cooled in air until they reached RT, and then grounded to fine powders of $Zn_xNi_{1-x}Fe_2O_4$ ($x = 0, 0.2, 0.4, 0.6, 0.8, 1$). Phosphate buffer saline (PBS) was prepared by using sodium monobasic (NaH_2PO_4) and dibasic (Na_2HPO_4) phosphates to reach a pH value of 7.

Physicochemical Characterization: FE-SEM (Zeis SupraTM 50, Oberkochen, Germany) was used to examine the shape and the size of the particles. Micro-Raman measurements were carried out (Renishaw, inVia Raman Microscope) to interpret the molecular vibrations of the materials. X-ray powder diffraction (PANalytical Empyrean diffractometer (Malvern Panalytical, Malvern, UK)) was used to identify the crystal structure of the materials; the XRD analysis of the powder was carried out using a Bragg–Brentano geometry and Cu Kα ($\lambda = 1.5418$ Å) radiation at 40 kV and 40 mA. The powder sample was investigated in a 2θ ranging from 15° to 70°, with a step size of $0.013° \text{ s}^{-1}$ and a time step of 30 s. UV–vis spectroscopy was performed on a Cary 5000 UV–vis–NIR spectrophotometer (Varian Instruments, Mulgrave, Australia) equipped with a DR apparatus. XPS experiments were conducted on a PHI 5000 Versaprobe spectrometer using a monochromatic Al Kα (1486.6 eV) X-ray source. An electron gun and an ion gun were used as a charge compensation system. Binding energy calibration was applied by setting the position of the adventitious sp^3 carbon component at 284.8 eV. Pass energies were set at 187.85 and 23.5 eV for the acquisition of survey and high-resolution spectra, respectively.

Electrodes Modification: Screen-printed electrodes with carbon WE (area 0.12 cm^2), carbon counter electrode (CE), and Ag/AgCl reference electrode (RE) were used as electrochemical sensors. Ferrite materials suspensions were prepared by adding 3 mg material in 1 mL (3:1 material to solvent ratio) of butanol and the solution was put in an ultrasonic bath for 30 min. SPCEs were modified by spreading 5 μL of material suspension on top of the carbon WE, dried overnight (drop-casting technique), and stored at RT.

Electrochemical Measurements: Electrochemical characterization through CV was performed under normal conditions using Bio-logic SP-300 potentiostat with surface-modified screen-printed electrodes as electrochemical sensors to detect paracetamol in 0.1M PBS at pH 6.9. The sensor was configured to sweep the voltage ranging from −0.6 to +0.8 V (vs Ag/AgCl). Cyclic voltammograms were recorded by dropping 100 μL solution of 1 mM paracetamol in 0.1 M PBS pH 6.9 on top of the electrochemical sensor. The redox currents and potentials were assessed after background correction through the peak analysis option present in EC-Lab. CV was performed to study the effect of scan rate on voltammograms by varying the scan rate from 50 to 300 mV s^{-1} (step size of 50 mV s^{-1}). Calibration of sensors was made by using CV at different concentrations of paracetamol ranging from 0.5 to 3 mM in steps of 0.5 mM at a scan rate of 100 m V s^{-1} and the sensitivity of the sensors was retrieved by taking the slope of the calibration. LOD was calculated using the sensitivity and the standard deviation of blank measurements. Repeatability and reproducibility were checked by performing the CV 5 times on the same sample and on three different samples for each type of sensor, respectively. All the data processing and plotting were performed using MATLAB.

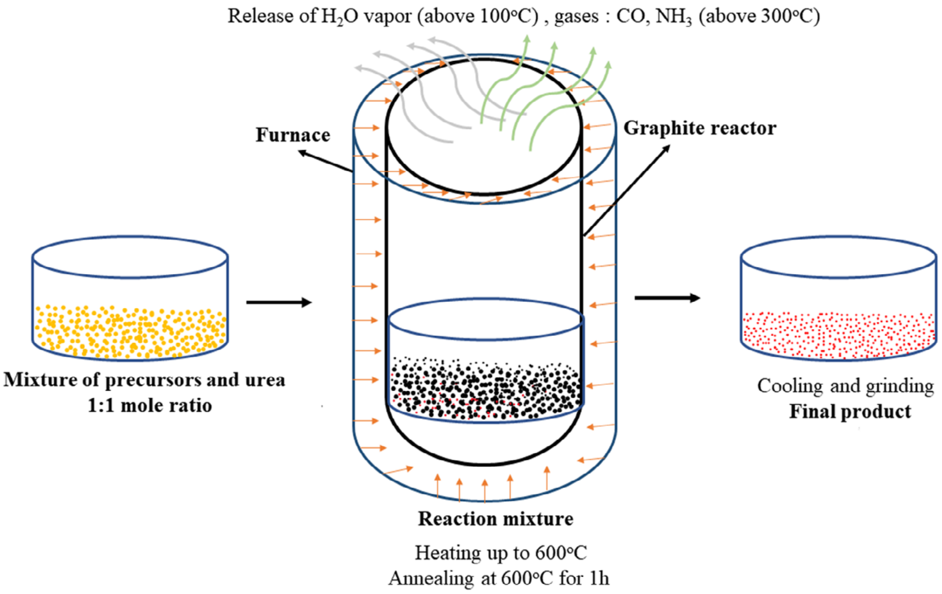

Scheme 1. Autocombustion synthesis of Zn–Ni ferrites.

Supporting Information

Supporting Information is available from the Wiley Online Library or from the author.

Acknowledgements

The authors thank Politecnico di Torino for the open access funding within the CRUI-CARE agreement.

Conflict of Interest

The authors declare no conflict of interest.

Author Contributions

M.M. and M.B. conceived the work and M.M. wrote the manuscript; M.M. synthesized the materials; M.B. and M.M. performed the Raman spectroscopic measurements and data interpretation; M.B. collected FE-SEM images; M.M. and M.B. analyzed the images; M.R. and E.P. performed XRD measurements and data analysis; N.B., M.M., and B.B. did the DR UV–vis spectroscopy and interpretation; M.E. performed XPS measurements; M.E. and M.M. did the data analysis; M.M. performed the electrochemical measurements and data analysis; and M.B., S.C., and A.T. supervised the work and revised the manuscript.

Data Availability Statement

The data that support the findings of this study are available from the corresponding author upon reasonable request.

Keywords

bandgap, ferrites, nanoparticles, rate constants, sensitivity, spinel

Received: May 9, 2023
Revised: July 26, 2023

---

[1] P. R. Graves, C. Johnston, J. J. Campaniello, *Mater. Res. Bull.* **1988**, *23*, 1651.
[2] G. R. Ferracutti, M. F. Gargiulo, M. L. Ganuza, E. A. Bjerg, S. M. Castro, *Mineral. Petrol.* **2015**, *109*, 153.
[3] V. Šepelák, K. D. Becker, *Mater. Sci. Eng. A* **2004**, *375–377*, 861.
[4] Y. Köseoğlu, A. Baykal, F. Gözüak, H. Kavas, *Polyhedron* **2009**, *28*, 2887.
[5] T. Prabhakaran, J. Hemalatha, *Ceram. Int.* **2014**, *40*, 3315.
[6] P. Sivakumar, R. Ramesh, A. Ramanand, S. Ponnusamy, C. Muthamizhchelvan, *J. Alloys Compod.* **2013**, *563*, 6.
[7] M. H. Mahmoud, A. M. Elshahawy, S. A. Makhlouf, H. H. Hamdeh, *J. Magn. Magn. Mater.* **2013**, *343*, 21.
[8] A. Kremenović, B. Antić, P. Vulić, J. Blanuša, A. Tomic, *J. Magn. Magn. Mater.* **2017**, *426*, 264.
[9] Y. Ge, Z. Wang, M. Yi, L. Ran, *Trans. Nonferrous Met. Soc. China* **2019**, *29*, 1503.
[10] D. Mohanty, P. Mallick, S. K. Biswal, B. Behera, R. K. Mohapatra, A. Behera, S. K. Satpathy, *Mater. Today Proc.* **2020**, *33*, 4971.
[11] S. Feng, W. Yang, Z. Wang, *Mater. Sci. Eng. B* **2011**, *176*, 1509.
[12] A. C. F. M. Costa, E. Tortella, M. R. Morelli, M. Kaufman, R. H. G. A. Kiminami, *J. Mater. Sci.* **2002**, *37*, 3569.
[13] Z. K. Karakaş, R. Boncukcuoğlu, İ. H. Karakaş, M. Ertuğrul, *J. Magn. Magn. Mater.* **2015**, *374*, 298.
[14] P. Sivakumar, R. Ramesh, A. Ramanand, S. Ponnusamy, C. Muthamizhchelvan, *Mater. Res. Bull.* **2011**, *46*, 2204.
[15] K. N. Nithyayini, M. N. K. Harish, K. L. Nagashree, *Electrochim. Acta* **2019**, *317*, 701.
[16] D. Ghanbari, M. Salavati-Niasari, M. Ghasemi-Kooch, *J. Industr. Eng. Chem.* **2014**, *20*, 3970.
[17] M. A. S. Amulya, H. P. Nagaswarupa, M. R. A. Kumar, C. R. Ravikumar, S. C. Prashantha, K. B. Kusuma, *Appl. Surf. Sci. Adv.* **2020**, *1*, 100023.
[18] Y. Sharma, N. Sharma, G. V. S. Rao, B. V. R. Chowdari, *Electrochim. Acta* **2008**, *53*, 2380.
[19] X. Guo, X. Lu, X. Fang, Y. Mao, Z. Wang, L. Chen, X. Xu, H. Yang, Y. Liu, *Electrochem. Commun.* **2010**, *12*, 847.
[20] X. Zhao, L. Mao, Q. Cheng, J. Li, F. Liao, G. Yang, L. Xie, C. Zhao, L. Chen, *Chem. Eng. J.* **2020**, *387*, 124081.
[21] V. S. Kumbhar, A. D. Jagadale, N. M. Shinde, C. D. Lokhande, *Appl. Surf. Sci.* **2012**, *259*, 39.
[22] F. Zhong, Z. Li, Y. Luo, C. Chen, C. Zhou, L. Lin, G. Cai, C. Au, L. Jiang, *Chem. Eng. J.* **2021**, *425*, 131822.
[23] X. Montero, F. Tietz, D. Sebold, H. P. Buchkremer, A. Ringuede, M. Cassir, A. Laresgoiti, I. Villarreal, *J. Power Sources* **2008**, *184*, 172.
[24] J. M. Gonçalves, L. V. de Faria, A. B. Nascimento, R. L. Germscheidt, S. Patra, L. P. Hernández-Saravia, J. A. Bonacin, R. A. A. Munoz, L. Angnes, *Anal. Chim. Acta* **2022**, *1233*, 340362.
[25] T. Dippong, E. A. Levei, O. Cadar, *Nanomaterials* **2021**, *11*, 1560.
[26] C. Fan, L. Chen, R. Jiang, J. Ye, H. Li, Y. Shi, Y. Luo, G. Wang, J. Hou, X. Guo, *ACS Appl. Nano Mater.* **2021**, *4*, 4026.
[27] G. Kesavan, M. Pichumani, S.-M. Chen, C.-S. Ko, *Mater. Today Chem.* **2022**, *26*, 101045.
[28] J. N. Baby, B. Sriram, S.-F. Wang, M. George, *Chem. Eng. J.* **2022**, *435*, 134136.
[29] Y. Huang, Y. Tang, S. Xu, M. Feng, Y. Yu, W. Yang, H. Li, *Anal. Chim. Acta* **2020**, *1096*, 26.
[30] R. Liu, M. Lv, Q. Wang, H. Li, P. Guo, X. S. Zhao, *J. Magn. Magn. Mater.* **2017**, *424*, 155.
[31] L. Ning, X. Guan, J. Ma, M. Wang, X. Fan, G. Zhang, F. Zhang, W. Peng, Y. Li, *J. Alloys Compd.* **2018**, *738*, 317.
[32] P. Guo, L. Cui, Y. Wang, M. Lv, B. Wang, X. S. Zhao, *Langmuir* **2013**, *29*, 8997.
[33] Z. Shahnavaz, F. Lorestani, Y. Alias, P. M. Woi, *Appl. Surf. Sci.* **2014**, *317*, 622.
[34] S. Mondal, M. Kumari, R. Madhuri, P. K. Sharma, *Appl. Phys. A* **2017**, *123*, 494.
[35] A. Afkhami, H. Khoshsafar, H. Bagheri, T. Madrakian, *Anal. Chim. Acta* **2014**, *831*, 50.
[36] M. Kumar, B. E. K. Swamy, C. Sravanthi, C. M. P. Kumar, G. K. Jayaprakash, *Mater. Chem. Phys.* **2022**, *284*, 126087.
[37] P. Maji, R. B. Choudhary, *Mater. Chem. Phys.* **2017**, *193*, 391.
[38] D. Chu, F. Li, X. Song, H. Ma, L. Tan, H. Pang, X. Wang, D. Guo, B. Xiao, *J. Colloid Interface Sci.* **2020**, *568*, 130.
[39] L. Luo, Q. Li, Y. Xu, Y. Ding, X. Wang, D. Deng, Y. Xu, *Sens. Actuators B Chem.* **2010**, *145*, 293.
[40] E. W. Gorter, *Philips Res. Rep.* **1954**, *9*, 295.
[41] U. König, G. Chol, *J. Appl. Crystallography* **1968**, *1*, 124.
[42] N. N. Greenwood, A. Earnshaw, in *Chemistry Of The Elements*, Reed Educational And Professional Publishing Ltd, School of Chemistry, University of Leeds, Leeds, UK **1997**.
[43] A. Kumar, P. Sharma, D. Varshney, *Ceram. Int.* **2014**, *40*, 12855.
[44] A. Ahlawat, V. G. Sathe, *J. Raman Spectrosc.* **2011**, *42*, 1087.

[45] F. Nekvapil, A. Bunge, T. Radu, S. Cinta Pinzaru, R. Turcu, *J. Raman Spectrosc.* **2020**, *51*, 959.
[46] O. Yamashita, T. Ikeda, *J. Appl. Phys.* **2004**, *95*, 1743.
[47] O. N. Shebanova, P. Lazor, *J. Raman Spectrosc.* **2003**, *34*, 845.
[48] M. Rivero, A. del Campo, Á. Mayoral, E. Mazario, J. Sánchez-Marcos, A. Muñoz-Bonilla, *RSC Adv.* **2016**, *6*, 40067.
[49] J. P. Singh, R. C. Srivastava, H. M. Agrawal, R. Kumar, *J. Raman Spectrosc.* **2011**, *42*, 1510.
[50] K. D. Dahm, D. J. Dahm, in *Handbook of Near-Infrared Analysis* **2021**, pp. 27–43.
[51] H. Cai, G. C. Farrington, *J. Electrochem. Soc.* **1992**, *139*, 744.
[52] R. Yang, Z. Zhang, J. Wu, X. Li, L. Wang, *Kinetics Catal.* **2015**, *56*, 222.
[53] F. Goga, R. A. Bortnic, A. Avram, M. Zagrai, L. Barbu Tudoran, R. A. Mereu, *Materials* **2022**, *15*, 8713.
[54] X. Xu, A. K. Azad, J. T. S. Irvine, *Catal. Today* **2013**, *199*, 22.
[55] R. Dillert, D. H. Taffa, M. Wark, T. Bredow, D. W. Bahnemann, *APL Mater.* **2015**, *3*, 104001.
[56] P. Makuła, M. Pacia, W. Macyk, *J. Phys. Chem. Lett.* **2018**, *9*, 6814.
[57] K. Dileep, B. Loukya, N. Pachauri, A. Gupta, R. Datta, *J. Appl. Phys.* **2014**, *116*, 103505.
[58] M. Srivastava, A. K. Ojha, S. Chaubey, A. Materny, *J. Alloys Compd.* **2009**, *481*, 515.
[59] M. Sultan, R. Singh, *J. Phys. D Appl. Phys.* **2009**, *42*, 115306.
[60] B. Delley, E. F. Steigmeier, *Appl. Phys. Lett.* **1995**, *67*, 2370.
[61] M. Singh, M. Goyal, K. Devlal, *J. Taibah Univ. Sci.* **2018**, *12*, 470.
[62] K.-F. Lin, H.-M. Cheng, H.-C. Hsu, L.-J. Lin, W.-F. Hsieh, *Chem. Phys. Lett.* **2005**, *409*, 208.
[63] A. M. Smith, S. Nie, *Acc. Chem. Res.* **2010**, *43*, 190.
[64] S. Klubnuan, S. Suwanboon, P. Amornpitoksuk, *Opt. Mater.* **2016**, *53*, 134.
[65] X. Yang, H. Xue, Q. Yang, R. Yuan, W. Kang, C.-S. Lee, *Chem. Eng. J.* **2017**, *308*, 340.
[66] Z. Li, J. Nie, J. Zhao, S. Yao, J. Wang, X. Feng, *J. Mater. Sci. Mater. Electron.* **2019**, *30*, 21416.
[67] G. Liu, X. Gao, K. Wang, D. He, J. Li, *Int. J. Hydrogen Energy* **2016**, *41*, 17976.
[68] K. Panwar, S. Tiwari, K. Bapna, N. L. Heda, R. J. Choudhary, D. M. Phase, B. L. Ahuja, *J. Magn. Magn. Mater.* **2017**, *421*, 25.
[69] N. McIntyre, M. Cook, *Anal. Chem.* **1975**, *47*, 2208.
[70] M. Etzi Coller Pascuzzi, A. J. W. Man, A. Goryachev, J. P. Hofmann, E. J. M. Hensen, *Catal. Sci. Technol.* **2020**, *10*, 5593.
[71] C. Fares, M. J. Tadjer, J. Woodward, N. Nepal, M. A. Mastro, C. R. Eddy, F. Ren, S. J. Pearton, *ECS J. Solid State Sci. Technol.* **2019**, *8*, Q3154.
[72] M. Madagalam, M. Bartoli, A. Tagliaferro, S. Carrara, *IEEE Sens. J.* **2021**, *21*, 11155.
[73] A. J. Bard, L. R. Faulkner, in *Electrochemical Methods Fundamentals And Applications*, Wiley, New York **2001**.
[74] T. J. Davies, C. E. Banks, R. G. Compton, *J. Solid State Electrochem.* **2005**, *9*, 797.
[75] I. Streeter, G. G. Wildgoose, L. Shao, R. G. Compton, *Sens. Actuators B Chem.* **2008**, *133*, 462.
[76] J. M. Savéant, in *Elements Of Molecular And Biomolecular Electrochemistry*, John Wiley & Sons, Hoboken, NJ **2006**.
[77] N. Elgrishi, K. J. Rountree, B. D. McCarthy, E. S. Rountree, T. T. Eisenhart, J. L. Dempsey, *J. Chem. Educ.* **2018**, *95*, 197.
[78] E. Laviron, *J. Electroanal. Chem. Interfacial Electrochem.* **1979**, *101*, 19.
[79] X. Kang, J. Wang, H. Wu, J. Liu, I. A. Aksay, Y. Lin, *Talanta* **2010**, *81*, 754.
[80] R. S. Nicholson, *Anal. Chem.* **1965**, *37*, 1351.
[81] A. D. McNaught, A. Wilkinson, in *IUPAC. Compendium Of Chemical Terminology*, Blackwell Science, Oxford **1997**.
[82] S. Carrara, C. Baj-Rossi, C. Boero, G. D. Micheli, *Electrochim. Acta* **2014**, *128*, 102.
[83] S. J. Yoon, S. H. Lee, K. H. Kim, K. S. Ahn, *Mater. Chem. Phys.* **2002**, *73*, 330.
[84] A. Šutka, K. A. Gross, *Sens. Actuators B Chem.* **2016**, *222*, 95.
[85] N. Ponpandian, P. Balaya, A. Narayanasamy, *J. Phys. Condens. Matter* **2002**, *14*, 3221.
[86] D. R. Patil, B. K. Chougule, *Mater. Chem. Phys.* **2009**, *117*, 35.
[87] C. Solís, S. Somacescu, E. Palafox, M. Balaguer, J. M. Serra, *J. Phys. Chem. C* **2014**, *118*, 24266.
[88] L. Yang, Y. Xie, H. Zhao, X. Wu, Y. Wang, *Solid-State Electron.* **2005**, *49*, 1029.
[89] A. Sutka, J. Zavickis, G. Mezinskis, D. Jakovlevs, J. Barloti, *Sens. Actuators B Chem.* **2013**, *176*, 330.
[90] A. A. Tahir, K. G. U. Wijayantha, *J. Photochem. Photobiol. A: Chem.* **2010**, *216*, 119.
[91] E. Burello, A. P. Worth, *Nanotoxicology* **2011**, *5*, 228.
[92] E. Burello, A. P. Worth, *WIREs Nanomed. Nanobiotechnol.* **2011**, *3*, 298.
[93] H. Zhang, Z. Ji, T. Xia, H. Meng, C. Low-Kam, R. Liu, S. Pokhrel, S. Lin, X. Wang, Y.-P. Liao, M. Wang, L. Li, R. Rallo, R. Damoiseaux, D. Telesca, L. Mädler, Y. Cohen, J. I. Zink, A. E. Nel, *ACS Nano* **2012**, *6*, 4349.
[94] S. Esposito, N. Ditaranto, G. Dell'Agli, R. Nasi, P. Rivolo, B. Bonelli, *ACS Omega* **2021**, *6*, 5379.
[95] L. Gomathi Devi, B. Narasimha Murthy, *Catal. Lett.* **2008**, *125*, 320.
[96] H. Kobayashi, T. Mori, K. Namba, Y. Nakato, *Solid State Commun.* **1994**, *92*, 249.
[97] M. Auffan, J. Rose, M. R. Wiesner, J.-Y. Bottero, *Environ. Pollut.* **2009**, *157*, 1127.
[98] T. Xia, Y. Zhao, T. Sager, S. George, S. Pokhrel, N. Li, D. Schoenfeld, H. Meng, S. Lin, X. Wang, M. Wang, Z. Ji, J. I. Zink, L. Mädler, V. Castranova, S. Lin, A. E. Nel, *ACS Nano* **2011**, *5*, 1223.
[99] T. Xia, M. Kovochich, M. Liong, L. Mädler, B. Gilbert, H. Shi, J. I. Yeh, J. I. Zink, A. E. Nel, *ACS Nano* **2008**, *2*, 2121.